



# Jet-related Excitation of the [C II] Emission in the Active Galaxy NGC 4258 with SOFIA

P. N. Appleton<sup>1</sup>, T. Diaz-Santos<sup>2</sup>, D. Fadda<sup>3</sup>, P. Ogle<sup>4</sup>, A. Togi<sup>5,6</sup>, L. Lanz<sup>7</sup>, K. Alatalo<sup>4</sup>, C. Fischer<sup>8</sup>, J. Rich<sup>9</sup>, and P. Guillard<sup>10,11</sup>

<sup>1</sup> IPAC, MC 100-22, Caltech, 1200 E. California Blvd., Pasadena, CA 91125, USA; [apple@ipac.caltech.edu](mailto:apple@ipac.caltech.edu)

<sup>2</sup> Nucleo de Astronomia de la Facultad de Ingenieria, Universidad Diego Portales, Av. Ejercito Libertador 441, Santiago, Chile

<sup>3</sup> SOFIA Science Center, USRA, NASA Ames Research Center, M.S. N232-12 Moffett Field, CA 94035, USA

<sup>4</sup> Space Telescope Science Institute, 3700 San Martin Drive, Baltimore, MD 21218, USA

<sup>5</sup> Department of Physics & Environmental Sciences, St. Mary's University, 1-Camino Santa Maria, San Antonio, TX 78228, USA

<sup>6</sup> Department of Physics and Astronomy, Trinity University, 1 Trinity Pl., San Antonio, TX 78212, USA

<sup>7</sup> Department of Physics and Astronomy, Dartmouth College, 6127 Wilder Laboratory, Hanover, NH 03755-3528, USA

<sup>8</sup> Deutsches SOFIA Institut, University of Stuttgart, D-70569 Stuttgart, Germany

<sup>9</sup> Carnegie Observatories, Carnegie Institute of Washington, Pasadena, CA, USA

<sup>10</sup> Institut Astrophysique de Paris, 98bis Boulevard Arago, F-75014 Paris, France

<sup>11</sup> Institut Universitaire de France, Ministère de l'Éducation Nationale, de l'Enseignement Supérieur et de la Recherche, 1 rue Descartes, 75231 Paris Cedex 05, France

Received 2018 September 4; revised 2018 October 15; accepted 2018 October 29; published 2018 December 12

## Abstract

We detect widespread [C II] 157.7  $\mu\text{m}$  emission from the inner 5 kpc of the active galaxy NGC 4258 with the SOFIA integral field spectrometer FIFI-LS. The emission is found to be associated with warm H<sub>2</sub>, distributed along and beyond the end of the southern jet, in a zone known to contain shock-excited optical filaments. It is also associated with soft X-ray hotspots, which are the counterparts of the “anomalous radio arms” of NGC 4258, and a 1 kpc long filament on the minor axis of the galaxy that contains young star clusters. Palomar CWI H $\alpha$  integral field spectroscopy shows that the filament exhibits non-circular motions within NGC 4258. Many of the [C II] profiles are very broad, with the greatest line width, 455 km s<sup>-1</sup>, observed at the position of the southern jet bow-shock. Abnormally high ratios of  $L([\text{C II}])/L(\text{FIR})$  and  $L([\text{C II}])/L(\text{PAH } 7.7 \mu\text{m})$  are found along and beyond the southern jet and in the X-ray hotspots. These are the same regions that exhibit unusually large intrinsic [C II] line widths. This suggests that the [C II] traces warm molecular gas in shocks and turbulence associated with the jet. We estimate that as much as 40% ( $3.8 \times 10^{39}$  erg s<sup>-1</sup>) of the total [C II] luminosity from the inner 5 kpc of NGC 4258 arises in shocks and turbulence (<1% bolometric luminosity from the active nucleus), the rest being consistent with [C II] excitation associated with star formation. We propose that the highly inclined jet is colliding with, and being deflected around, dense irregularities in a thick disk, leading to significant energy dissipation over a wide area of the galaxy.

*Key words:* galaxies: active – galaxies: jets – galaxies: ISM – infrared: galaxies

## 1. Introduction

NGC 4258 is a Seyfert 1.9 galaxy, where water vapor masers yielded the first high-accuracy determination of the mass of a supermassive black hole (SMBH; Greenhill et al. 1995; Miyoshi et al. 1995). The action of a jet is thought to be responsible for the “anomalous” radio-continuum spiral arms, which appear several kiloparsecs from the center and extend through the outer disk. These arms, which do not correlate with the galaxy’s underlying stellar spiral structure, are not well understood, but are somehow related to present or past jet activity that has triggered enhanced synchrotron radiation along the jet’s path and excited shocks and X-ray emission (van Albada & van der Hulst 1982). A tiny radio jet, highly inclined to the stellar disk of NGC 4258, is seen on the scale of milliarcseconds (0.3–3 pc; Cecil et al. 2000). An extrapolation of the radio jet outward from the center reveals two distinct optical “bow-shock-like” structures, seen faintly in H $\alpha$  emission, with different projected angular distances from the nucleus (Cecil et al. 2000; Wilson et al. 2001). The jet path and the interface zones are seen faintly at radio wavelengths, and the northern bow shock has an X-ray counterpart. This provides strong evidence that the jet is currently interacting with the host galaxy’s interstellar medium (ISM). In Figure 1, we mark the position angle of the radio jet (PA = 6°) as a black line extrapolated onto a narrow-band (F657N) H $\alpha$ -centered image

from the *Hubble Space Telescope* (HST) of the inner 3 kpc of the galaxy centered on the nucleus. The projected length of the jet is 74 arcsec = 2.6 kpc at an assumed distance of 7.3 Mpc.

Extensive Fabry–Perot spectrophotometric imaging of the entire galaxy in H $\alpha$  and [N II]  $\lambda$ 6583 was performed by Cecil et al. (1992). These observations showed that the inner jet is only part of the picture, because they discovered an extensive system of “braided” emission-line filaments over a large area southeast of the southern termination of the jet. The optical emission-line ratios in these braided structures were consistent with shocks.

The filaments, and the existence of the extensive radio and X-ray “anomalous arms,” whose inner orientation does not quite line up with the position angle of the jet, have led to several different ideas about the action of the jet. These include the possibility that the jet is precessing, and that it may have been pointing closer to the gas disk of the galaxy in the past (Cecil et al. 2000). Another model is that the jet is tilted by 30° to the disk plane, and that the bow shocks represent ends of the jet where they have penetrated into the low-density halo of the galaxy (Cecil et al. 2000; Wilson et al. 2001; Yang et al. 2007). In this model, shock waves produced in the halo gas by the jet propagate outward and collide with the denser disk gas, mirroring the jet within the gas disk. This creates the appearance of the X-ray and radio “arms,” which, because of

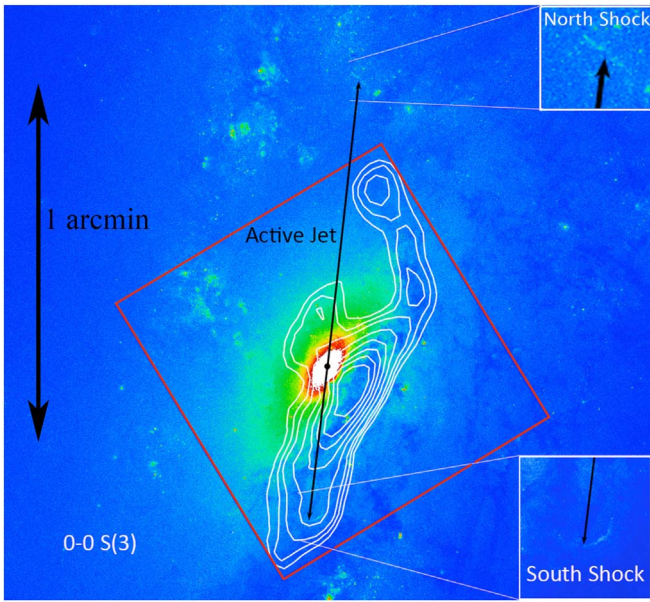


**Figure 1.** Central region of NGC 4258 from the *HST* F657N WFC3 (including the  $H\alpha$  line) in false colors with contours of the 0–0 S(3)  $9.7\ \mu\text{m}$  rotational  $H_2$  line from *Spitzer* observations (Ogle et al. 2014). The black line shows the extent of the jet that appears to have created faint  $H\alpha$  bow shocks at both ends of it (see insets and work of Cecil et al. 2000; Wilson et al. 2001). The southern extent of the  $H_2$  emission appears to coincide with the southern jet interface. The red box shows the extent of the *Spitzer* spectral mapping from which the contour map was derived. 1 arcmin at  $D = 7.3$  Mpc corresponds to 2.1 kpc.

the inclined viewing angle, leads to an offset in position angle between the jet and the disk shocks.

Ogle et al. (2014), using spectral mapping from the *Spitzer* Infrared Spectrograph (IRS), showed that the inner environs of the galaxy contain large amounts of warm  $H_2$  distributed along the inner anomalous arms. The warm temperature and large ratio of  $L(H_2)/L(\text{PAH})$  emission<sup>12</sup> are consistent with shock heating of the gas, presumably by the jet, a situation that is common in powerful radio galaxies (Ogle et al. 2007, 2010; Guillard et al. 2012b; Lanz et al. 2015, 2016). In Figure 1, we show the integrated emission from the rotational  $H_2$  0–0 S(3)  $9.7\ \mu\text{m}$  line superimposed on the *HST* image. It is particularly striking that the faint shock-like feature identified by Cecil et al. (2000) at the southern end of the jet appears to coincide with the extension of the warm  $H_2$  along that direction. This suggests that some of the  $H_2$  is being directly affected by the current jet. Unfortunately, the *Spitzer* IRS map did not cover the northern bow shock, although the gas seems more scattered in that direction.

The [C II]  $157.7\ \mu\text{m}$  fine-structure line has been shown through *Infrared Space Observatory* (ISO) and *Herschel* observations to be an excellent tracer of star formation in normal, Milky Way-type nearby galaxies. UV radiation from young stars heats molecular gas by photoelectric ejection of electrons from PAH molecules and small grains in photodissociation regions (PDRs; Draine 1978; Tielens & Hollenbach 1985; Hollenbach & McKee 1989). The warm  $H_2$  and neutral hydrogen then collisionally excite the ionized carbon. In addition, collisions with free electrons in highly ionized H II regions can also excite the [C II] transition (see Goldsmith et al. 2012).

<sup>12</sup> PAH refers to mid-IR polycyclic aromatic hydrocarbon bands, in this case the  $7.7\ \mu\text{m}$  broad complex.

In normal galaxies and in the extended disks of IR-luminous galaxies, this process forms the basis of the strong correlation between star formation and [C II] emission (see Malhotra et al. 2001; Díaz-Santos et al. 2014; Herrera-Camus et al. 2015, for recent reviews).

Shocks and turbulence can sometimes dominate over photoelectric heating, especially in diffuse intergalactic gas involved in high-speed galaxy collisions, for example in Stephan’s Quintet (Appleton et al. 2013). In the Taffy (UGC 12914/5) galaxy collision (Peterson et al. 2018), both warm  $H_2$  and H I were implicated in enhanced [C II] emission from the turbulent bridge created in the head-on collision of two galaxies (see also the case of HCG 57A; Alatalo et al. 2014). Similarly, powerful [C II] emission was observed in the radio galaxy 3C 326 and other radio galaxies (Guillard et al. 2015). Turbulent dissipation and shocks driven into the gas surrounding a radio jet are thought to be the main heating process for the  $H_2$ , which can also collisionally excite the [C II] transition.

Our current paper concentrates on what can be learned from observations by the Stratospheric Observatory for Infrared Astronomy (SOFIA; Erickson & Davidson 1993) of the [C II]  $157.7\ \mu\text{m}$  far-IR (FIR) fine-structure line as an additional probe of the conditions in the gas close to the nucleus and jet in NGC 4258. We also present observations with the Palomar 5 m telescope and the optical IFU *Cosmic Web Imager* (PCWI; Rahman et al. 2006) to help provide further insight into the conditions in the areas covered by the SOFIA observations. We will discuss the implications of these observations for understanding possible feedback effects of radio jets on the host galaxy’s ISM.

We assume a distance to NGC 4258 of 7.3 Mpc based on a Virgocentric-corrected radial velocity of  $531\ \text{km s}^{-1}$  and a Hubble constant of  $73\ \text{km s}^{-1}\text{Mpc}^{-1}$ . One arcminute at this assumed distance corresponds to a linear scale of 2.1 kpc.

## 2. Observations

### 2.1. SOFIA Observations

We observed NGC 4258 with the Field-Imaging Far-Infrared Line Spectrometer (FIFI-LS) on the SOFIA 2.5 m telescope on 2016 March 4 (obsID = 04\_0017\_1; Flight 285; Cycle 4), and again on 2017 February 28 (obsID = 05\_0014\_2,3; Flight 379; Cycle 5). FIFI-LS is an infrared integral field spectrometer with two channels capable of covering a wavelength range from 50 to  $125\ \mu\text{m}$  (blue channel) and  $105\text{--}200\ \mu\text{m}$  (red channel) (Looney et al. 2000; Klein et al. 2014; Fischer et al. 2018). FIFI-LS has an array of  $5 \times 5$  spatial pixels (spaxels) covering a field of view of  $30 \times 30\ \text{arcsec}^2$  in the blue ( $6 \times 6\ \text{arcsec}^2$  spaxels) and  $60 \times 60\ \text{arcsec}^2$  ( $12 \times 12\ \text{arcsec}^2$  spaxels) in the red. The red channel was centered on the [C II]  $\lambda 157.741\ \mu\text{m}$  line at a heliocentric velocity of  $450\ \text{km s}^{-1}$ , with a wavelength coverage of  $\pm 0.5\ \mu\text{m}$  ( $\sim 1900\ \text{km s}^{-1}$  overall coverage). At this wavelength, FIFI-LS has a velocity resolution of  $260\ \text{km s}^{-1}$ . The blue channel was centered on the redshifted [O III]  $\lambda 88.35\ \mu\text{m}$  line, but no line was detected. The [O III] upper limits are given at the end of this section, and are discussed further in Section 3.1.

Observations were made in 10 cycles (30 s per cycle) of a five-point dither pattern. The 3 arcsec offsets for each dither correspond to one-half and one-quarter of a spaxel in the blue and red detectors respectively and allow a better reconstruction of the spatial point-spread function. A two-point symmetric

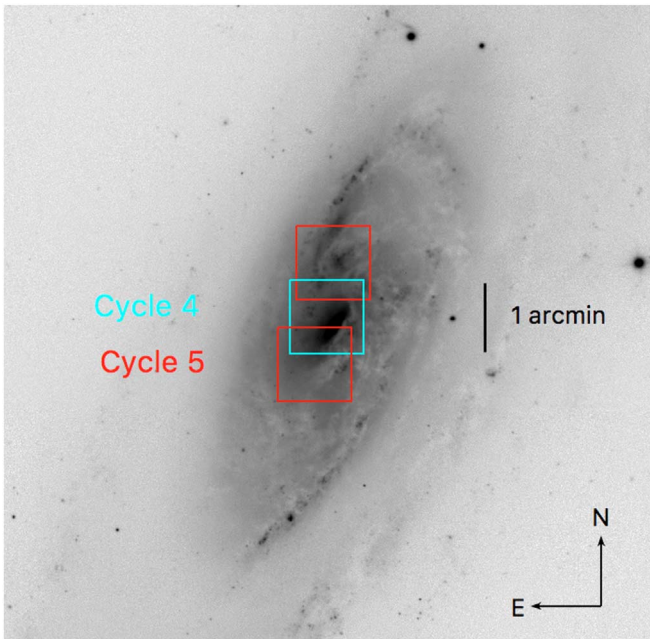


**Figure 2.** Coverage of the SOFIA Cycles 4 (cyan) and 5 (red) FIFI-LS observations overlapped on a Sloan Digital Sky Survey (SDSS)  $g$ -band image of the whole galaxy. The targeted areas were chosen to include the ISM immediately surrounding the jet (see Cecil et al. 2000; Wilson et al. 2001). To provide context and scale, the Cycle 4 coverage box is approximately the same scale as the displayed area in the *HST* image of Figure 1.

chopping mode was used with a chop throw of 180 arcsec and a chopping frequency of 2 Hz. The nodding cycle (pattern ABBA) alternately placed the galaxy in the A or B position every 30 s. Figure 2 shows the placement of the footprints of the FIFI-LS red array (the primary array for this observation) on an image of the galaxy. The total effective “on source” integration time was 32.2 minutes, in Cycle 4 (targeting the central pointing) and 32.7 and 18.4 minutes on the north and south pointings respectively for Cycle 5.

The FIFI-LS flux calibration is based on a series of multi-flight measurements using Uranus, Mars, and Callisto as well as single reference observations during individual flights. As a result, the calibration over the multiple flights has been shown to be constant at the 10% level. Line observations are further corrected for atmospheric absorption and telluric features by the SOFIA FIFI-LS team using ATRAN models (Lord 1992).<sup>13</sup> The correction is performed using expected values of the water vapor at the altitude of the observation. This adds a further 10% flux uncertainty. Based on these factors, we assume that the uncertainty in the absolute flux calibration for the integrated line fluxes is  $\pm 20\%$ .

To improve the quality of the final data cubes, we discarded approximately 4% of the observations made during abrupt changes of altitude and highly variable sky conditions. We also masked (red channel only) a column of five spaxels that are badly illuminated. Without this important correction, the high values of the flat at the position of these spaxels considerably increased the noise of the final coadded cube, leading to significant edge-effects in the maps. The removal of these offending pixels had a significant positive effect on the quality of the final data cube.

Finally, for the analysis of the data cube, we used SOSPEX, a Python GUI software (Fadda & Chambers 2018) available as an Anaconda package.<sup>14</sup> In particular, the software was used to define the continuum level and subtract it from the cube to study the distribution of the [C II] line flux. Typical  $2.5\sigma$  noise levels for a  $200 \text{ km s}^{-1}$  wide line were approximately  $1.5 \times 10^{-17}$  and  $4 \times 10^{-17} \text{ W m}^{-2} \text{ beam}^{-1}$  respectively for the [C II] and [O III] data cubes. These are close to the values predicted by the FIFI-LS exposure time calculator for average conditions.

## 2.2. Palomar Cosmic Web Imager (PCWI) Observations

As a follow-up to the SOFIA observations, we have begun a project to map a large part of the inner few square arcminutes of NGC 4258 with the PCWI. PCWI (Rahman et al. 2006) consists of a long-slit spectrograph that is fed by a  $60 \times 40 \text{ arcsec}^2$  integral field unit (IFU) to provide a 2D field of view sampled by  $24 \times 2.5 \text{ arcsec}$  reflective slits. The instrument was used at the Cassegrain focus of the Hale 5 m Palomar telescope on 2018 March 13. Observations of a spectrophotometric standard (for bandpass calibration) and a single pointing on and off NGC 4258 were made. Due to bad weather, we took advantage of a 50 minute clear window to perform a shallow observation (600 s on and 600 s off target). This provided a useful snapshot of the conditions in the inner galaxy, especially the H II regions seen in the [C II] minor-axis filament near the nucleus. We used the yellow grating, covering  $500 \text{ \AA}$  centered at  $6440 \text{ \AA}$ , with a spectral resolution of  $5000$  ( $60 \text{ km s}^{-1}$ ). These data were processed through a standard PCWI data reduction pipeline, which allowed for the removal of cosmic rays, calibration of wavelength and flux, and final cube building. The fully calibrated on and off cubes were subtracted to produce the final data cube. The initial World Coordinate System (WCS) astrometry (based on the telescope pointing) was corrected by aligning the peak  $\text{H}\alpha$  absorption seen against the nucleus with the compact active galactic nucleus (AGN) seen in the *HST* image. The pixel scale of the final data cube was  $2.5 \times 1 \text{ arcsec}^2$ .

## 3. Results

### 3.1. Distribution of [C II] Emission

We show in Figure 3(a) the large-scale distribution of the integrated [C II] emission superimposed on the *HST* image of NGC 4258, and a zoom-in on the nuclear region in Figure 3(b). The extent of the jet is also shown.

The [C II] emission shows several main features, including an elongated filament that extends approximately along the minor axis of the galaxy toward the northeast, as well as several concentrations to the north and south of the nucleus. The minor-axis filament encompasses a bright distorted loop of compact  $\text{H}\alpha$ -emitting star clusters, seen especially in Figure 3(b). A second, brighter ridge, displaced by 20 arcsec from the nucleus, extends along the direction of the jet and beyond it to the southeast. Two extended regions of emission are also seen north of the nucleus, straddling the northern jet bow shock. The eastern component is associated with an extension of one of the normal spiral arms, but the western component is correlated with an X-ray enhancement seen in the

<sup>13</sup> [ntrs.nasa.gov/archive/nasa/casi.ntrs.nasa.gov/19930010877.pdf](https://ntrs.nasa.gov/archive/nasa/casi.ntrs.nasa.gov/19930010877.pdf)

<sup>14</sup> <http://www.sofia.usra.edu/sites/default/files/AAS231wide.pdf> and [github.com/darioflute/sospex](https://github.com/darioflute/sospex).

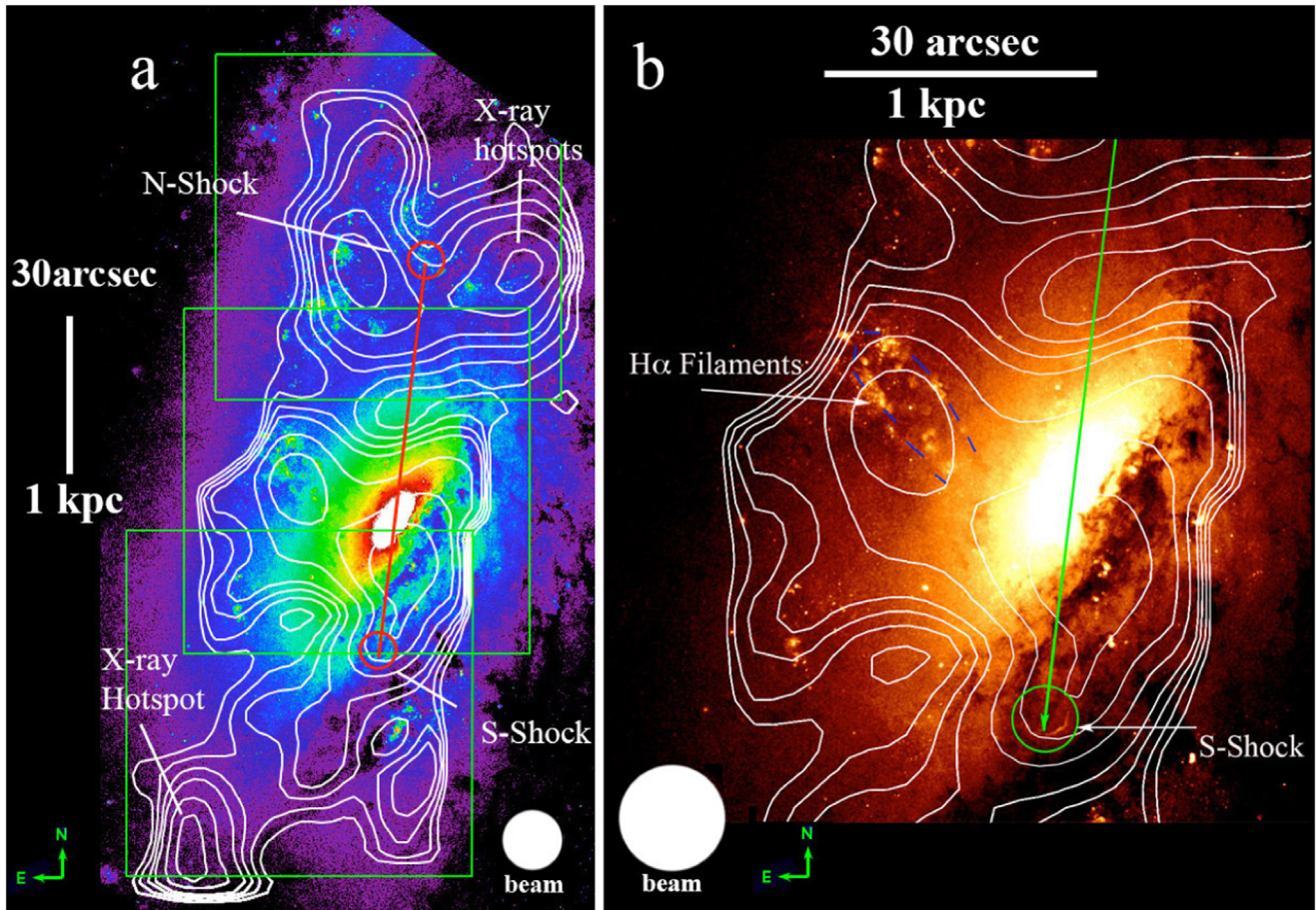


**Figure 3.** (a) Contours of the [C II] emission superimposed on a false-color representation of the *HST* F657N WFC3 image over the inner 3 kpc of NGC 4258, and (b) a zoom-in on the [C II] emission associated with the minor-axis optical emission, with the same background image as (a) but with a different color table and stretch. Note the loop-like distribution of H $\alpha$  emission (blue dotted lines) associated with the minor-axis [C II] contours and the elongation of the [C II] emission along the southern jet. The jet is marked with a line ending in two circles, which surround the bow-shock structures visible as faint features in the H $\alpha$  image (see Cecil et al. 2000; Wilson et al. 2001, for more details). The green squares show the footprint of the observed regions with SOFIA. The SOFIA beam at 158  $\mu\text{m}$  (FWHM 13 arcsec) is shown as white filled circles. Contour levels are  $(1.5, 2, 2.5, 3, 4, 5, 6) \times 10^{-18} \text{ W m}^{-2} \text{ pixel}^{-1}$ , and the lowest contour is approximately twice the rms noise, which varies with the line width along the line of sight. Each pixel is  $2 \times 2 \text{ arcsec}^2$ .

northern part of the inner anomalous emission (Wilson et al. 2001). A similar bright [C II] emission feature is seen to the extreme southeast of the nucleus, at the edge of the mapping zone. This latter emission is not associated with any obvious optical continuum source but coincides with more anomalous X-ray emission. Finally, we detect a fainter concentration of [C II] emission to the south of the nucleus.

The [O III] 88  $\mu\text{m}$  line was not detected, even from the nucleus of the galaxy at a  $2.5\sigma$  level of  $4 \times 10^{-17} \text{ W m}^{-2} \text{ beam}^{-1}$ . At the nucleus, this corresponds to an upper limit of  $<0.3$  for the ratio of  $L(\text{[O III]})/L(\text{[C II]})$  and  $<0.001$  for  $L(\text{[O III]})/L(\text{FIR})$ . This is well within the scatter of points in AGNs described by Herrera-Camus et al. (2018), and is clearly not within the range of more powerful AGNs discussed in that paper, which have  $L(\text{[O III]})/L(\text{[C II]})$  ratios greater than unity.

### 3.2. Velocity Structure of the [C II] Emission

To further explore the main features of the emission we show in Figure 4 contours of the [C II] emission from the channel maps superimposed on both the *HST* F657N images (upper panels) and the *Chandra* X-ray images (lower panels). The emission is integrated over  $50 \text{ km s}^{-1}$  intervals, starting at a heliocentric velocity of  $200 \text{ km s}^{-1}$  and ending at  $750 \text{ km s}^{-1}$ .

The lowest velocity emission ( $200 \text{ km s}^{-1}$ ) begins in a clump along the major axis of the galaxy at the extreme southeast and shows some extension along a dust lane at higher velocities.

This southernmost feature is seen in many channels, indicating a large velocity dispersion, and seems to be associated with a bright knot of X-ray emission at the point where the X-ray emission bends eastward. From this point onward, the velocity field does not behave like that of a regular edge-on disk galaxy, which should show a progression of emission with increasing velocity approximately along the major axis. Instead, in the velocity range  $200\text{--}500 \text{ km s}^{-1}$ , we see emission associated with a ridge of gas southeast of the nucleus and emission associated with the southern jet.

Emission is also detected associated with the minor-axis filament ( $250\text{--}600 \text{ km s}^{-1}$ ). Given that the systemic velocity of the galaxy based on the maser disk is  $471 \pm 4 \text{ km s}^{-1}$ , it is clear that the majority of the minor-axis filament emission is blueshifted (we will discuss this further in Section 6). The easternmost component of the two [C II] emission regions straddling the northern jet bow shock begins to appear around  $350 \text{ km s}^{-1}$ , remains until  $600 \text{ km s}^{-1}$ , and is far from the major axis. The western component appears at higher velocities (around  $550 \text{ km s}^{-1}$ ) and extends west and north up to

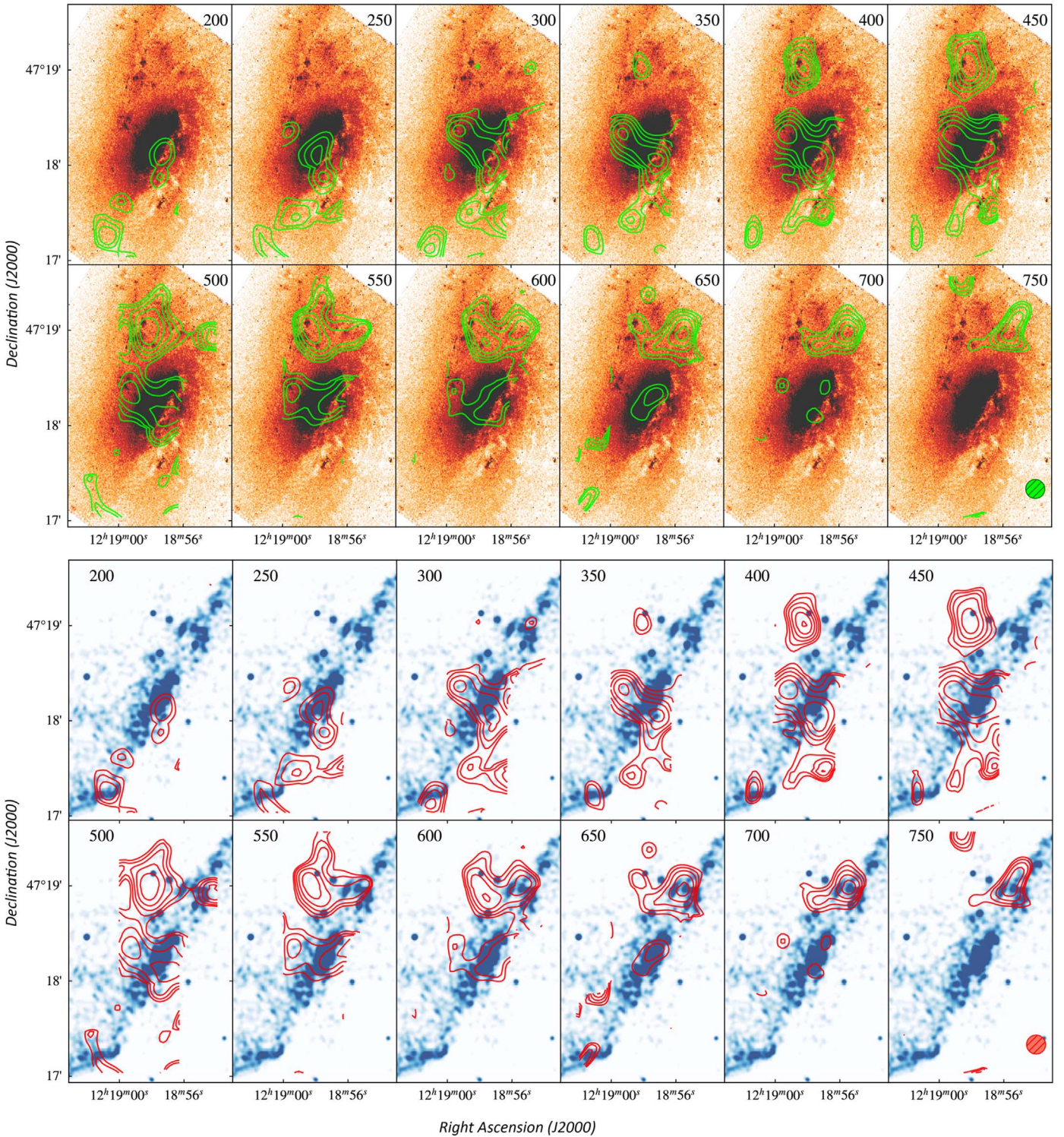


**Figure 4.** Channel maps showing the [C II] emission as a function of heliocentric radial velocity in slices of  $50 \text{ km s}^{-1}$  superimposed on false-color versions of the *HST* F657N WFC3 image (upper panels) and the 0.5–8 keV *Chandra* X-ray image (lower panels). Velocities (in  $\text{km s}^{-1}$ ) are marked at the top of each panel. The shaded circle in the bottom corner of each image shows the FWHM beam size of SOFIA. The contour levels are 0.1, 0.12, 0.15, 0.18, 0.23  $\text{Jy pixel}^{-1}$ . Each pixel is  $2 \times 2 \text{ arcsec}^2$ . Since the velocity resolution is  $260 \text{ km s}^{-1}$ , adjacent channel maps are not fully independent of each other.

$750 \text{ km s}^{-1}$ , where it disappears. This latter emission component is aligned with the diffuse X-ray emission in the extreme northwest. In summary, except for the extreme ends of the observed velocity range, where the emission seems roughly associated with X-ray emission, the velocity field of the inner parts of the [C II] emission is dominated by peculiar motions in

the southern jet, extended emission to the southeast, and the minor-axis filament.

Another way of looking at the velocity field is to create contours of the intensity-weighted mean velocity of the emission shown in Figure 5(a). We show contours of the [C II] integrated surface density superimposed on a color-coded

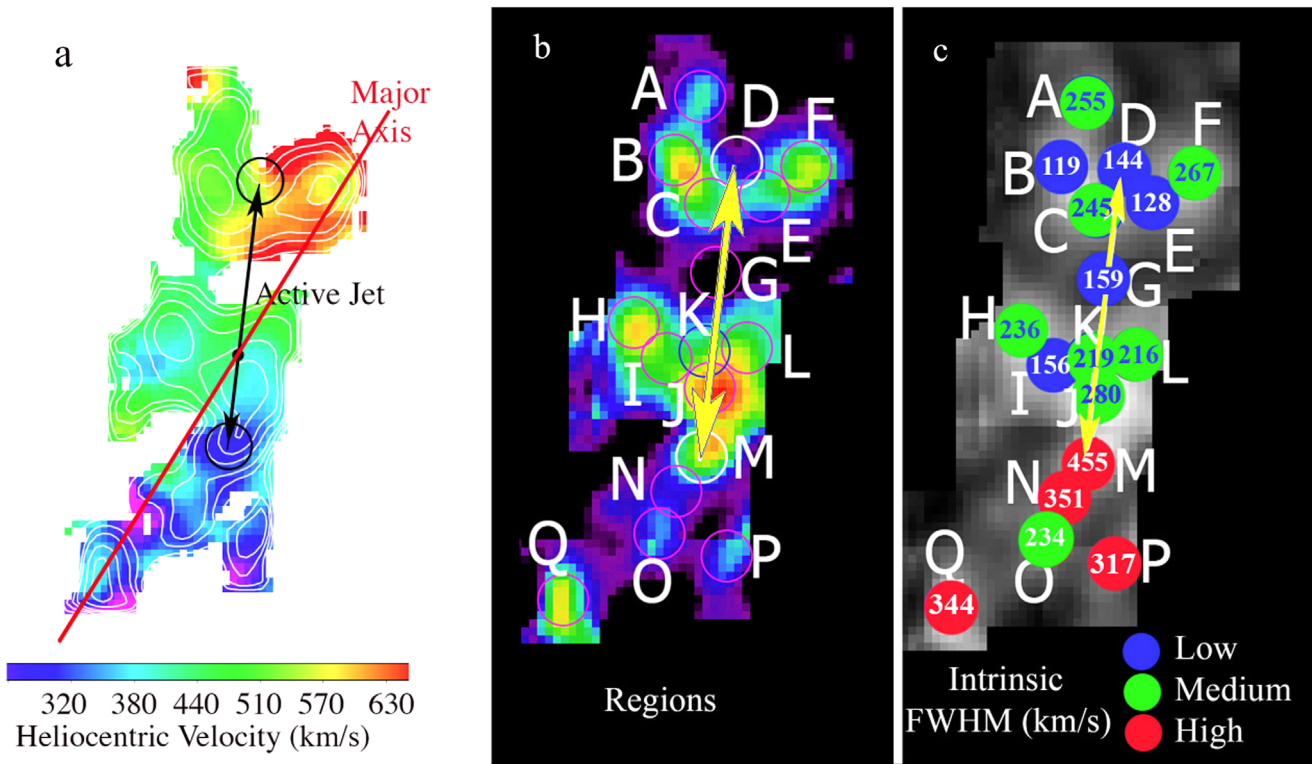


**Figure 5.** (a) Color-coded intensity-weighted velocity map of the [C II] emission in units of heliocentric velocity ( $\text{km s}^{-1}$ ) derived from the first moment of the data cube. White contours show the integrated [C II] surface density. The velocity moment map was masked according to a signal-to-noise cut of 3. The black filled circle marks the nucleus. The black line and open circles denote the position and end-points of the jet, which has a projected length of  $74 \text{ arcsec} = 2.6 \text{ kpc}$  at an assumed distance of  $7.3 \text{ Mpc}$ . (b) Extraction regions (purple circles) superimposed on the integrated [C II] surface density map (see Table 1 for their properties). The two white circles (Regions D and M) represent extractions coinciding with the ends of the jet (yellow arrow). The nucleus lies at the center of the blue circle (Region K). (c) Deconvolved FWHM [C II] line widths (assuming a spectral resolution of  $260 \text{ km s}^{-1}$ ) derived from Gaussian fits to Regions A through Q in  $\text{km s}^{-1}$  labeled on each region (see Table 1). Red filled circles show the highest values ( $\text{FWHM} > 300 \text{ km s}^{-1}$ ), green intermediate ( $200 < \text{FWHM} < 300 \text{ km s}^{-1}$ ), and blue the lowest values ( $\text{FWHM} < 200 \text{ km s}^{-1}$ ). Note that the regions with highest velocity dispersion are all south of the nucleus, with the highest value at the end of the southern jet (Region M).

image of the velocity field for clarity. The map shows that the gas kinematics in the center of NGC 4258 are very peculiar. There is a strong north–south gradient in the velocity field from the nucleus (around  $450\text{--}470 \text{ km s}^{-1}$ ) to the point at the tip of the southern jet where the velocities are quite low ( $280\text{--}300 \text{ km s}^{-1}$ ). These velocities are not consistent with rotation of the galaxy. In the northern part of the [C II] mapped region, the highest systemic velocities are seen in the northwestern extended structure, while the most distant emission directly north of the nucleus has a lower, almost uniform, systemic velocity over much of its extent. The velocity field is strikingly similar to that seen in  $\text{H}\alpha$  in the Fabry–Perot spectrophotometric imaging data of Cecil et al. (1992). For example, the high velocities seen to the north and west of the northern jet bow shock are well reproduced in the ionized gas, showing quite similar structure. Also, along the southern jet, and parallel to the major axis, the ionized gas displays low velocities (going down to  $300 \text{ km s}^{-1}$ ) following the same pattern as Figure 5(a). It is in this southern region that Cecil et al. (1992) mention an increase in  $[\text{NII}]/\text{H}\alpha$  that is characteristic of shock excitation.

To help quantify the properties of the lines and their profiles, we define in Figures 5(b) and (c) a set of extraction regions, marked A to Q, superimposed on the [C II] surface density map. The regions are circles with  $13 \text{ arcsec}$  diameters, the size of the telescope beam at  $158 \mu\text{m}$ . In Table 1, we show the

measured kinematic and integrated [C II] properties derived by fitting a Gaussian to the extracted spectra. Columns include the extracted line flux, area, central velocity, and observed line widths. We also present the intrinsic line widths (corrected for a Gaussian instrument profile of  $\text{FWHM} = 260 \text{ km s}^{-1}$ ).<sup>15</sup>

In Figure 5(c), we show the intrinsic line width of the extracted spectra as a function of position, color-coded by velocity width. Most of the extracted profiles are unusually broad, with the lowest at  $119 \text{ km s}^{-1}$ , occurring at the position of the brightest northern clump B. The gas with the highest velocity dispersion ( $455 \text{ km s}^{-1}$ ) occurs at the position of the bow shock at the tip of the southern jet (Region M), with high values also in Regions N, P, and Q. A clear trend emerges from the figure. Most of the gas with lower velocity dispersion (blue and green circles) occurs in the north and within the minor-axis filament, whereas all the red circles ( $\text{FWHM} > 300 \text{ km s}^{-1}$ ) occur to the south in the southern jet and to the southeast. We note that the velocity dispersion in the ionized gas measured with the Fabry–Perot imaging described previously shows multiple velocity components in these regions, with each broad line reaching a maximum of  $80 \text{ km s}^{-1}$ . We will discuss these so-called “braided filaments” later in the paper.

<sup>15</sup> <http://www.sofia.usra.edu/science/proposing-and-observing/data-products/data-resources>

**Table 1**  
[C II] Properties of the Extracted Regions (Uncertainties in Parentheses)

Region	Line Flux ( $10^{-17}$ W m $^{-2}$ )	Area (arcsec $^2$ )	$V_{\text{cen}}$ (km s $^{-1}$ )	$\Delta V_{\text{obs}}^{\text{a}}$ (km s $^{-1}$ )	$\Delta V_{\text{d}}^{\text{b}}$ (km s $^{-1}$ )	$f_{\text{C II}}(\text{FIR})$ ( $10^{-14}$ W m $^{-2}$ )	$\frac{L([\text{C II}])}{L(\text{FIR})}$ ( $10^{-2}$ )	8 $\mu\text{m}$ PAH Flux $^{\text{c}}$ ( $10^{-15}$ W m $^{-2}$ )	$\frac{L([\text{C II}])}{L(\text{PAH})}$ ( $10^{-2}$ )
A	11.2 (1.2)	128	498 (12)	364 (12)	255 (12)	1.19 (0.12)	0.95 (0.14)	1.95 (0.19)	5.8 (0.8)
B	16.1 (1.0)	128	490 (6)	286 (6)	119 (6)	2.60 (0.26)	0.62 (0.07)	5.99 (0.60)	2.9 (0.3)
C	16.4 (1.3)	128	549 (9)	357 (9)	245 (9)	1.31 (0.13)	1.25 (0.16)	1.99 (0.20)	8.2 (1.0)
D	9.2 (1.0)	128	529 (11)	297 (11)	144 (11)	1.31 (0.13)	0.70 (0.11)	1.82 (0.18)	5.4 (0.8)
E	11.5 (1.1)	128	636 (9)	290 (9)	128 (9)	1.29 (0.13)	0.89 (0.12)	1.98 (0.20)	5.8 (0.8)
F	16.5 (2.0)	128	636 (14)	373 (14)	267 (14)	0.95 (0.09)	1.74 (0.27)	1.71 (0.17)	10.6 (1.7)
G	0.1 (0.05)	128	494 (19)	305 (19)	159 (19)	1.16 (0.12)	0.31 (0.07)	0.81 (0.08)	4.9 (1.2)
H	16.5 (1.1)	128	415 (7)	351 (7)	236 (7)	1.73 (0.17)	0.96 (0.11)	3.92 (0.39)	4.2 (0.5)
I	13.0 (0.8)	128	415 (6)	303 (6)	156 (6)	1.94 (0.19)	0.67 (0.08)	2.41 (0.24)	5.7 (0.7)
J	16.5 (2.6)	128	405 (18)	382 (18)	280 (18)	2.25 (0.22)	0.73 (0.14)	3.54 (0.35)	4.7 (0.9)
K	12.7 (1.5)	128	431 (13)	340 (13)	219 (13)	3.06 (0.31)	0.42 (0.06)	8.42 (0.84)	1.6 (0.2)
L	12.2 (1.3)	128	461 (12)	338 (12)	216 (12)	2.61 (0.26)	0.47 (0.07)	3.52 (0.35)	3.6 (0.5)
M	15.4 (1.4)	128	283 (15)	524 (15)	455 (15)	1.18 (0.12)	1.31 (0.18)	1.32 (0.13)	11.7 (1.6)
N	9.9 (1.0)	128	330 (15)	437 (15)	351 (15)	0.99 (0.10)	1.0 (0.14)	1.16 (0.12)	8.5 (1.2)
O	9.2 (0.7)	128	302 (9)	350 (9)	234 (9)	0.55 (0.05)	1.69 (0.22)	0.43 (0.04)	23.8 (3.1)
P	9.2 (1.7)	128	338 (24)	410 (24)	317 (24)	0.34 (0.03)	2.71 (0.57)	0.16 (0.02)	59.5 (12.5)
Q	11.0 (1.4)	128	273 (18)	431 (18)	344 (18)	0.16 (0.02)	6.70 (1.10)	0.06 (0.01)	206.6 (33.9)

**Notes.**

<sup>a</sup> FWHM from observed line profile.

<sup>b</sup> Intrinsic FWHM after deconvolution with a Gaussian instrument profile of FWHM 260 km s $^{-1}$ .

<sup>c</sup> 8  $\mu\text{m}$  PAH fluxes estimated from *Spitzer* IRAC band 4 fluxes, correcting the contributions from stars using band 1 fluxes and the formalism of Helou et al. (2004). Fluxes assume an effective bandwidth for the 8  $\mu\text{m}$  filter of 2.9  $\mu\text{m}$ .

#### 4. [C II] to FIR Ratios across the Face of NGC 4258

In Figure 6(a), we show the integrated line emission of [C II] (white contours) superimposed on a map of the far-IR emission derived from *Herschel* archival images at 70 and 160  $\mu\text{m}$ , which were smoothed to the same spatial resolution as the [C II] maps. The IR photometry was fitted with a modified blackbody ( $\beta = 1.8$ ) and then integrated from 41 to 121  $\mu\text{m}$  to obtain the far-IR flux and luminosity. It is clear from the map that, although we detect strong emission from the nucleus in the far-IR, the peak of the [C II] is offset approximately 10 arcsec to the southwest of the nucleus, and extends along the direction of the southern jet. In the north, there is an approximate correspondence between the far-IR emission and the [C II], but in the south it is less obvious. In Figure 6(b), we show the ratio of the [C II] line luminosity to the far-IR luminosity  $L[\text{C II}]/L(\text{FIR})$  (expressed as a percentage) as contours superimposed on [C II] surface density map. In most places the ratio has values of  $\sim 0.5\%$ – $1\%$ , but to the south and the extreme northwest, these values are significantly higher.

To put all this in context, we compare in Figure 7 the spatially resolved [C II] properties of NGC 4258 with observations of other galaxies from the Great Observatories All-sky LIRG Survey (GOALS; Armus et al. 2009). The GOALS sample is useful because these galaxies encompass a wide range of FIR<sup>16</sup> properties, and bridge the gap between relatively quiescent sources and (ultra)luminous infrared galaxies (ULIRGs and LIRGs; Díaz-Santos et al. 2017). They also include spatially resolved extranuclear regions as well as nuclei. The plot illustrates the well-documented trend between the ratio of [C II]/FIR and FIR luminosity and luminosity density,  $\Sigma_{\text{FIR}}$ . It has been demonstrated that at high FIR

luminosity, the ratio of [C II] to FIR continuum decreases. This so-called [C II] deficiency is an effect that has been identified since the early days of observations of LIRGS with *ISO* (Malhotra et al. 1997, 2001). Recently, *Herschel* studies have shown that the [C II]/FIR ratio is more tightly anticorrelated with the IR luminosity density of galaxies (Díaz-Santos et al. 2013, 2017; Lutz et al. 2016; Smith et al. 2017; Herrera-Camus et al. 2018). Several explanations have been put forward for the drop in [C II] power in areas of very high star formation rate density. A common explanation for this effect is that as the UV radiation field per hydrogen atom (characterized as  $G_0/n_{\text{H}}$ ) increases in highly compact starburst regions, dust particles responsible for the FIR emission become progressively more charged. This inhibits the ability of the small grains and PAH molecules to emit photoelectrons, which in turn reduces the excitation of the molecular gas that triggers the [C II] 157.7  $\mu\text{m}$  transition in PDRs (Tielens & Hollenbach 1985; Wolfire et al. 1990; Malhotra et al. 1997; Kaufman et al. 1999; Negishi et al. 2001; Stacey et al. 2010).

However, a more likely explanation for the effect is an increase in the dust-to-gas opacity in dust-bounded H II regions, where the average ionization parameter is also higher (Voit 1992; González-Alfonso et al. 2004; Abel et al. 2009; Graciá-Carpio et al. 2011). Díaz-Santos et al. (2013) were able to show that there is a clear relationship between the increase in the [C II]/FIR deficiency and the average dust temperature of galaxies as well as with  $\Sigma_{\text{FIR}}$ , which is consistent with a boost of the ionization parameter even for pure star-forming regions (see also Fischer et al. 2014; Cormier et al. 2015; Herrera-Camus et al. 2018). Indeed, Díaz-Santos et al. (2017) demonstrated that the  $G_0/n_{\text{H}}$  ratio is positively correlated with the IR luminosity surface density of galaxies when  $\Sigma_{\text{FIR}} \gtrsim 5 \times 10^{10} L_{\odot}$ . As the GOALS galaxies show in Figure 7, at low values of FIR surface density, the [C II]/FIR ratio flattens to an asymptotic value of  $\sim 1\%$ . This is consistent with a low UV

<sup>16</sup> The definition of far-IR flux used in the GOALS study is identical to that used in this paper.

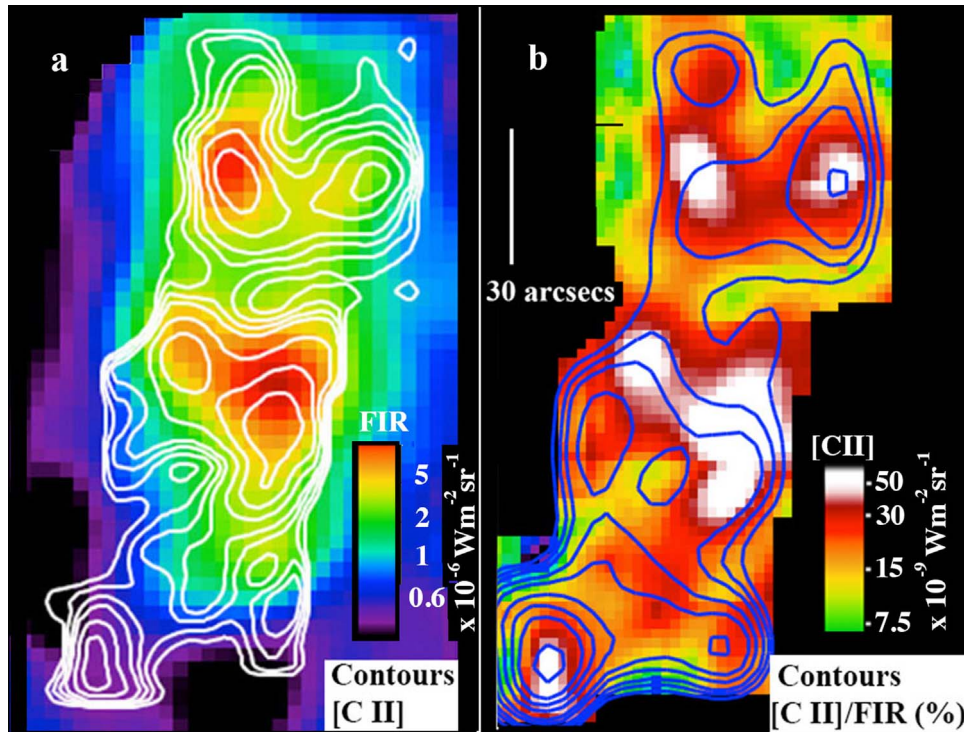


**Figure 6.** (a) Contours of  $L([\text{C II}])$  emission superimposed on a color image of  $L(\text{FIR})$ . Contours are the same units as in Figure 3. (b) Contours of  $L([\text{C II}])/L(\text{FIR})$ , expressed as a percentage, superimposed on an image of the  $[\text{C II}]$  surface density. Contour levels are 0.5%, 0.75%, 1%, 2%, 3%, 4%, 5%, 6%, 7%, and 8%.

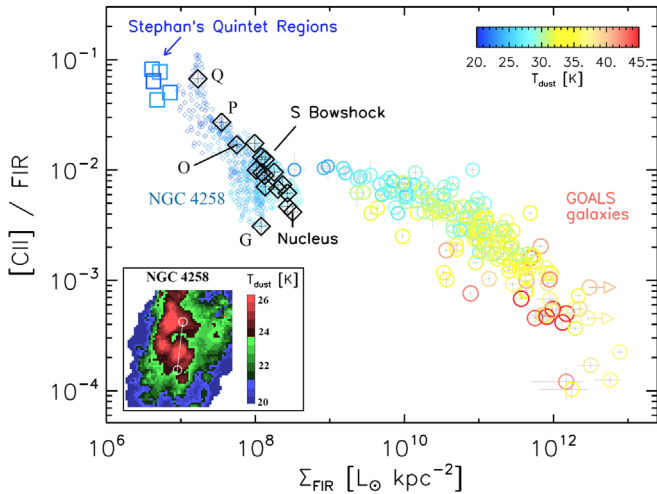


**Figure 7.** Ratio of  $L([\text{C II}])/L(\text{FIR})$  as a function of far-IR luminosity surface density. The circles are from the GOALS sample (Díaz-Santos et al. 2017). The small blue diamonds (left side of figure) are derived from the maps of NGC 4258, and the larger black diamonds show the values from the extracted regions A–Q in Table 1. The large blue squares are from the turbulent and shocked gas filament in the compact group Stephan’s Quintet (Appleton et al. 2013). All of the points on the figure (except the black diamonds) are color-coded according to the dust temperature, from very warm galactic nuclei (45 K, red) to cool intergalactic gas (20 K, dark blue). The inset in the bottom left corner shows the dust color temperature derived from the *Herschel* photometry smoothed to the same resolution as the SOFIA data. The white line and circles show the orientation and end-points of the jet. Note that the minor-axis filament and nucleus show a warmer dust temperature than the surroundings. The color bar for the inset covers a smaller range than the main figure.

radiation field and more neutral (less strongly ionized) PAHs. Similar trends are seen by other authors for normal nearby galaxies (e.g., Malhotra et al. 2001) and also at high redshift (e.g., Spilker et al. 2016).

In Figure 7, we also plot the points obtained for NGC 4258 both from the extraction regions A–Q and pixel-by-pixel across the map. As might be expected, for a galaxy classified as Seyfert 1.9, the nucleus of NGC 4258 shows a mild decrement relative to the majority of GOALS points at the same FIR surface density. Similar mild decrements have been found in Seyfert galaxy nuclei by Herrera-Camus et al. (2018), where the strength of the decrement was found to be dependent on the X-ray power of the AGN. The ionization conditions near the nucleus are likely to be responsible for this effect, either by changing the ionization parameter or by the direct impact of X-ray emission from the accretion disk, which can cause [C III] (or higher) ionization states at the expense of [C II] (Langer & Pineda 2015). Perhaps a little more surprising is that the lowest [C II]/FIR ratio is not in the nucleus but occurs just north of it, at position G (see Figure 5(b)). This is at a minimum in the [C II] surface density along the northern jet and may represent a volume that has been depleted by the jet, perhaps leading to a lower gas density there. If so, the low value of [C II]/FIR may imply that the gas is exposed directly to UV or X-ray emission from the nuclear accretion disk without much attenuation.

Although in Figure 7 we see a concentration of NGC 4258 data points around  $\Sigma_{\text{FIR}} \sim 10^8 L_{\odot} \text{ kpc}^{-2}$  and  $[\text{C II}]/\text{FIR} \sim 0.01$ , there is a significant deviation from the extrapolated values from GOALS. Aside from the nucleus and Region G, which have low values of [C II]/FIR, there is a tail of points in NGC 4258 going to high values of the ratio. The points associated with the gas south of the nucleus, Regions O, P, and Q, have the largest values of [C II]/FIR, and in the case of Region Q they are similar to those values found in the well studied Stephan’s Quintet shocked gas filament (Appleton et al. 2013). It has been demonstrated that low-velocity, mildly irradiated, magnetic C-shocks (with velocities typically less than  $10 \text{ km s}^{-1}$ ) driven into molecular gas can generate strong

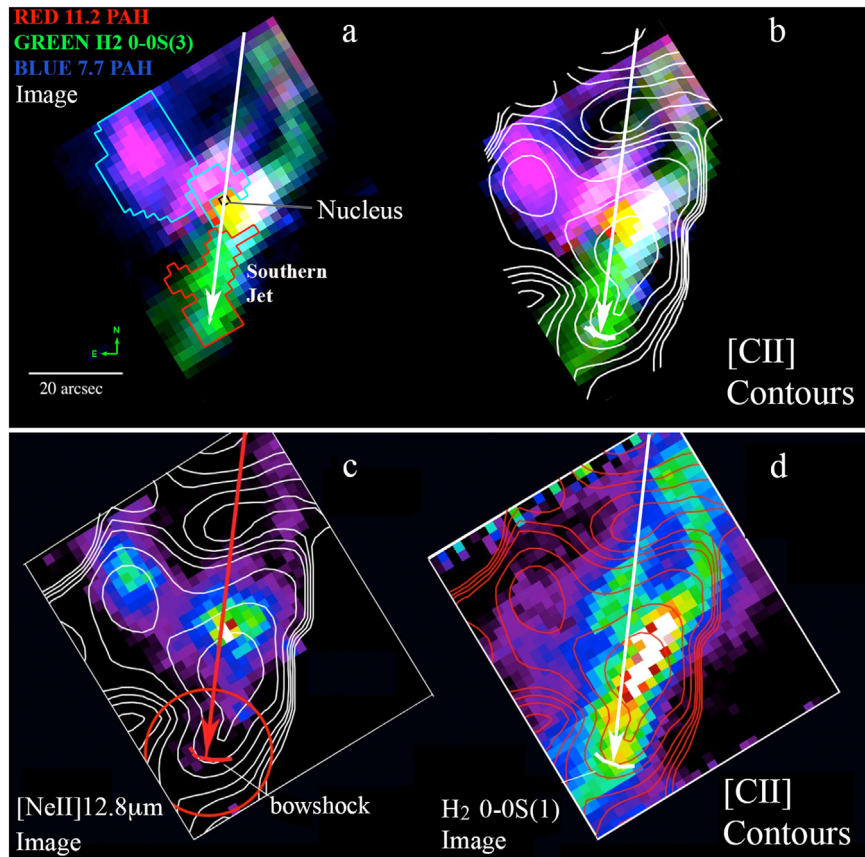


**Figure 8.** (a) *Spitzer* IRS color-coded image of the integrated emission from PAH  $11.2 \mu\text{m}$  (red),  $\text{H}_2$  0–0 S(3)  $9.7 \mu\text{m}$  (green), and PAH  $7.7 \mu\text{m}$  (blue) derived from line fitting with MPF (see Section 4.1) based on a CUBISM low-resolution spectral map. The blue and red boxes show the areas dominated by PAH and  $\text{H}_2$  line emission respectively. Note that the minor-axis filament is dominated by PAH emission, whereas the emission south of the nucleus is dominated by warm  $\text{H}_2$  emission along the southern jet (white arrow). (b) The SOFIA [C II] integrated emission contours superimposed on the same image. (c) Contours of [C II] emission superimposed on a *Spitzer* IRS image of the [Ne II]  $12.8 \mu\text{m}$  ionized gas. (d) The same contours superimposed on the map of the 0–0 S(1)  $17.0 \mu\text{m}$  molecular hydrogen line.

[C II] emission (see modeling of Lesaffre et al. 2013), and these seem to be responsible for shocks in that system (Appleton et al. 2017). In NGC 4258, optical spectroscopic evidence of faster shocks, driven into gas in the area of our regions N, O, P, and Q, has already been presented by Cecil et al. (1992). As the multiphase model of Guillard et al. (2009) has shown, fast shocks rapidly decay into low-velocity molecular shocks, which can heat the warm  $\text{H}_2$ , as well as creating pockets of hot X-ray-emitting gas where the pre-shock density was already low. As shown in Figure 8(d), the *Spitzer* observations show that warm  $\text{H}_2$  emission is observed all along the southern extension of the jet as far as Region Q. It is plausible that this warm  $\text{H}_2$  provides a collisional partner with carbon atoms to generate [C II] emission (Goldsmith et al. 2012). It is important to note that the increase in [C II]/FIR along regions O, P, and Q and the steep negative slope of the points for NGC 4258 in Figure 7 largely reflect the falling value of the FIR surface density with radial distance from the center of the galaxy (Figure 6(a)) and not necessarily an increase in excitation. For the shock interpretation of the [C II] emission, the [C II] and IR luminosity density (from mainly large grains) would not be expected to be correlated. Since the surface density of [C II] slowly falls and then rises again with distance from the center of the galaxy, high values of [C II]/FIR merely reflect different underlying (uncorrelated) distributions of the two quantities. On the other hand, for a PDR, [C II] and FIR emission will be

highly correlated, and such high values of [C II]/FIR would imply an unusually large photoelectric heating efficiency.

#### 4.1. What Excites the [C II] Transition in the Center of NGC 4258?

The center of NGC 4258 was spectrally mapped using the *Spitzer* IRS instrument, and results were shown in Ogle et al. (2014). We processed these data through CUBISM (Smith et al. 2007), and further analyzed them with the Multi-Purpose Fitter (MPF; P. M. Ogle et al. 2018, in preparation) cube-fitting software to extract line maps. Figure 8(a) and (b) show an RGB-coded representation of three spectral features seen in the IRS spectra, namely the  $7.7$  and  $11.2 \mu\text{m}$  PAH and the strong 0–0 S(3)  $\text{H}_2$  line. Figure 8(a) shows a clear result: the minor-axis filament, seen in both the *HST* image and the [C II] emission, is strongly dominated by PAH emission, whereas the area containing the southern jet is almost completely dominated by warm molecular hydrogen. The nucleus shows a mixture of both kinds of emission (in yellow). Strong  $\text{H}_2$  emission is seen to the northwest of the nucleus, but it is also mixed with PAH emission. This strong segregation between the minor-axis filament and the southern arm of the jet is evidence that two different heating mechanisms are present in the center of NGC 4258. The minor-axis filament is mainly dominated by star formation, whereas the southern jet is dominated by strong

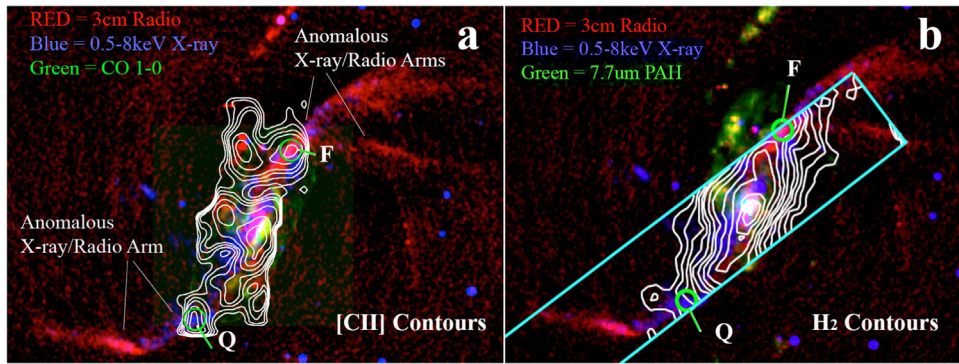


**Figure 9.** (a) [C II] integrated emission contours superimposed on an RGB color composite showing 3 cm radio emission (red), X-ray emission (blue), and CO 1–0 cold molecular gas (green). The radio and X-ray emission together emphasize the anomalous emission. Note the correspondence between [C II] emission at Regions F and Q (green circles) with the anomalous emission to the northwest and southeast corners of the mapped area. (b) Contours of 0–0 S(1) 17  $\mu\text{m}$  H<sub>2</sub> emission superimposed on a three-color underlying image, but this time showing radio (red), X-ray (blue), and 7.7  $\mu\text{m}$  PAH emission (green). We again mark Regions F and Q (green circles). The extent of the IRS (Long-Low module) spectral mapping by *Spitzer* is denoted by the cyan box.

mid-IR H<sub>2</sub> emission, devoid of star formation. Ogle et al. (2014) argued that the radio jet in NGC 4258, like many other known cases of powerful H<sub>2</sub> emission (e.g., a class of galaxies called molecular hydrogen emission galaxies (MOHEGs; Ogle et al. 2010)), is the heating source for the warm molecular gas. The close spatial correspondence between the warm H<sub>2</sub> and the southern jet, shown in Figures 1 and 8, supports this view.

The [C II] emission (white contours of Figure 8(b)) is associated with both the PDR-dominated minor-axis filament and the shock-heated gas along the southern jet, as well as with a mix of both processes at the center and to the northwest of the nucleus. This is the first time that [C II] emission has been directly resolved and clearly associated with shocked and turbulent gas in an AGN system, although other cases of shock-excited [C II] emission have been found in the radio galaxy 3C 326 (Guillard et al. 2015) and in intergalactic gas in both Stephan’s Quintet (Appleton et al. 2013, 2017) and the Taffy bridge (Peterson et al. 2018). Figure 8(c) shows how the ionized gas (in this case [Ne II] 12.8  $\mu\text{m}$  emission) again favors the nucleus and minor-axis filament, but not the southern jet, in contrast to the warm H<sub>2</sub>, shown in Figure 8(d) in the 0–0 S(1) 17  $\mu\text{m}$  line from *Spitzer*. The lack of strong ionized emission along the southern jet suggests that free electrons in H II regions are not responsible for the correlation between the [C II] emission and the southern jet.

We overlay in Figure 9(a) the [C II] emission contours on an RGB multicolor image showing 3 cm radio, 0.5–8 keV X-ray, and CO 1–0 emission (Krause et al. 2007; Laine et al. 2010). The red and blue colors emphasize the anomalous arm emission (Cecil et al. 2000; Wilson et al. 2001; Yang et al. 2007), except for some regions to the north, which are part of the normal spiral arms in the galaxy. The green color represents the CO 1–0 emission, which correlates with the southern jet. Faint CO emission is also found along the minor-axis filament. Figure 9(b) shows a similar background image, but this time the green color represents the 8  $\mu\text{m}$  IRAC image, which is dominated by PAH emission. The contours in this panel show the 0–0 S(1) 17  $\mu\text{m}$  emission from warm molecular hydrogen. Both Regions Q and F fall in the envelope of warm molecular hydrogen. Again a striking similarity is observed between the distribution of [C II] emission and the brighter H<sub>2</sub> emission south and southeast of the nucleus.

In Figure 9, we observe that both Regions Q and F coincide with peaks in the radio and X-ray emission of the anomalous

arms. Region F is quite elongated along the northern X-ray structure at velocities of 650–750 km s<sup>−1</sup> (Figure 4) and is close to a bifurcation point in the anomalous emission. Region Q, which seems brighter in X-rays and weak in H<sub>2</sub>, is an extension of a series of braided H $\alpha$  filaments associated with shocks by Cecil et al. (1992). Both Q and F extend to the edge of the area mapped by SOFIA, and it is likely that the emission extends further. The relatively bright [C II] emission in the absence of star formation, the large velocity dispersion of the gas (especially Region Q), and the position of both clumps F and Q near extended X-ray enhancements may indicate that the gas is shock-heated. However, the relative faintness of the 0–0 S(1) line at the position of Region Q is a puzzle, given that it is one of the brighter [C II] areas mapped by SOFIA. Unfortunately this region was not covered by the *Spitzer* IRS Short-Low detectors, which would have allowed us to determine whether it is dominated by much hotter H<sub>2</sub> than the other regions. For example, if the temperature was higher than 1000 K, the brightest H<sub>2</sub> emission would be shifted from transitions involving the lowest rotational energy levels to much higher rotational and rovibrational transitions, which emit at much shorter IR wavelengths than those that were observed.

#### 4.2. [C II]/PAH Ratios

Since the IRS Short-Low modules sensitive to PAH emission only cover a fraction of the area mapped by SOFIA, we used archival *Spitzer* IRAC 3.6 and 8  $\mu\text{m}$  images of NGC 4258 to create a large-scale map of the PAH 7.7  $\mu\text{m}$  feature using the method outlined by Helou et al. (2004). The IRAC 3.6  $\mu\text{m}$  image is used to correct for stellar emission in the 8  $\mu\text{m}$  PAH-dominated band. After smoothing the image to the same resolution as the SOFIA [C II] image, we extracted the 7.7  $\mu\text{m}$  complex PAH fluxes from each of the regions presented in Figure 5(b). The fluxes and the [C II]/PAH ratio are presented in Table 1. In Figure 10(a), we plot the ratio of [C II]/PAH as a function of FIR surface density. The plot shows a strong anticorrelation between [C II]/PAH and the IR surface density. This is not expected if the [C II] primarily arises in low-density PDRs, since the strength of both the PAH emission (which is UV-excited in star formation regions) and the [C II] emission should stay approximately constant with IR surface density. Furthermore, many points lie at unusually high values of [C II]/PAH ratio. These have been color-coded as red

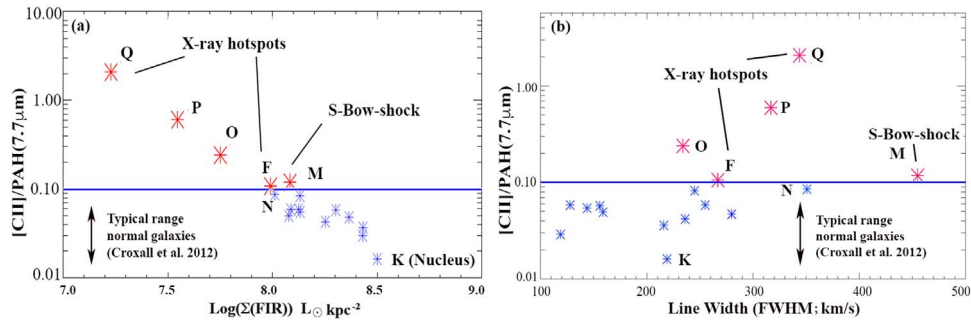


**Figure 10.** (a) Ratio of  $L([C II])/L(PAH)$  plotted against the far-IR luminosity surface density. We indicate with red and blue stars those regions where  $L([C II])/L(PAH)$  is above and below 0.1 respectively. (b) Using the same symbols for the points, we show the  $L([C II])/L(PAH)$  ratio plotted against the line width (FWHM corrected for instrumental broadening). Note that the red starred points have some of the broadest lines observed, including the most extreme, Region M, which coincides with the bow-shock structure at the end of the southern jet.

stars. Among the positions that show strong  $[C II]/PAH$  ratios there are many of the points south of the nucleus, including position M, which is at the end of the southern jet, and Region Q, which is very extreme. Regions Q and F coincide with the X-ray counterparts of the anomalous radio emission. Moreover, in Figure 10(b), when we plot the  $[C II]/PAH$  ratio against the line width of the  $[C II]$ , we notice that most of the points with high values of  $[C II]/PAH$  ratio have broad lines.

The broad lines suggest the presence of turbulent gas. In the intergalactic filament in Stephan’s Quintet, it was observed that the broadest  $[C II]$  line widths corresponded to gas containing the warmest  $H_2$ , providing a strong case for turbulence and shocks within a multiphase medium (Appleton et al. 2017). We note that the broad  $[C II]$  lines do not necessarily imply large shock velocities in the  $H_2$  component that triggers the  $[C II]$  emission. In a multiphase medium, large volumes of the gas can be stirred by the action of the jet, creating a turbulent cascade that drives energy to small scales and low velocities. The broad lines seen in NGC 4258 and in Stephan’s Quintet suggest large-scale stirring, which can lead to a multitude of small-scale low-velocity shocks spread throughout the velocity phase-space and spatially averaged across the telescope beam. The models of Lesaffre et al. (2013) show that  $[C II]$  emission as strong as the rotational  $H_2$  lines can arise in mildly UV-irradiated gas in C-shocks with velocities of up to  $10 \text{ km s}^{-1}$ . Such magnetic shocks may well be present near the radio jets.

Croxall et al. (2012), in a study of nearby galaxies, argued that the  $[C II]/PAH$  ratio is a good measure of the efficiency of the photoelectric heating of the ISM by UV radiation, showing lower scatter across the galaxies than  $[C II]/FIR$ . They found that  $L([C II] + [O I] 63 \mu m)/L(PAH)$  and  $L([C II])/L(PAH)$  were remarkably constant over a range of non-nuclear conditions, with average values of 6% and 3%–4% respectively, both with small scatter (an exception was in the nuclei of both NGC 4559 and NGC 1097, where there was a decrease seen in  $[C II]/PAH$ ; this is similar to that observed in NGC 4258). The strength of the  $[O I] 63 \mu m$  line in NGC 4258 is unknown since it is blocked by telluric absorption. Regardless, the high values of the  $[C II]/PAH$  ratio, in regions M, N, O, P, and Q imply an unrealistically high photoelectric efficiency if the  $[C II]$  originates in PDRs (e.g., Habart et al. 2003; Beirão et al. 2012). This, taken together with the previous similar behavior in the  $[C II]/FIR$  ratio, is consistent with the idea that shocks and turbulent kinematics play an important role in enhancing the  $[C II]$  emission. We note that in the scenario in which  $[C II]$  emission is boosted by shock-heated  $H_2$ , there is no expected correlation between  $[C II]$  and PAH emission.

Indeed PAHs could even be destroyed in shocks, as is suspected in the case of the intergalactic filament in Stephan’s Quintet (Appleton et al. 2006; Cluver et al. 2010). This would further increase the ratio of  $[C II]/PAH$  in mixed PDR–shock regions.

If we conservatively consider those areas with  $[C II]/PAH$  ratios  $>10\%$  to be inconsistent with the low efficiency of photoelectric heating of gas in PDRs, the percentage of  $[C II]$  emission arising from non-PDR processes compared with the total (integrating over the  $[C II]$  mapped region) is  $\sim 40\%$ . Although collisions between carbon atoms and neutral hydrogen could trigger  $[C II]$  emission, a recent HI map (C. Mundell 2018, personal communication) does not show a strong correlation between HI and  $[C II]$  emission throughout most of the inner parts of NGC 4258, especially in the areas containing the high  $[C II]/PAH$  ratios. Potentially ionized gas could contribute to the excitation of the  $[C II]$  emission, although we believe that this is minimal in the inner galaxy. We will explore the relationship between the various gas phases ( $[C II]$ , HI, CO, and ionized gas) in NGC 4258 in a forthcoming paper. In the next section, we discuss the more likely scenario of how the jet may be capable of creating shocks and turbulence over such a large area of the southern  $[C II]$ -emitting regions in Section 6.

## 5. Comparison with Jet Power and Soft X-Ray Emission from Shocks

Yang et al. (2007) performed a very extensive X-ray study of NGC 4258 and estimated the jet power based on the accretion rate onto the black hole measured by Neufeld & Maloney (1995) to be  $4 \times 10^{41} \text{ erg s}^{-1}$ . This is likely to be a lower limit since it excludes the possible contribution to the jet power from the black hole spin. The accretion rate may also be underestimated (see Section 7.1). Yang et al. (2007) estimate the soft X-ray luminosity in the anomalous inner arms to be  $4 \times 10^{39} \text{ erg s}^{-1}$ . If we assume that those areas with  $[C II]/PAH$  ratios  $>0.1$  are places where  $[C II]$  arises from post-shock cooling gas, we can sum the line luminosity for those regions (M, O, P, Q, and F) to provide a total  $[C II]$  line luminosity of  $3.8 \times 10^{39} \text{ erg s}^{-1}$ . Therefore, the soft X-ray power and  $[C II]$  line cooling rate each contribute 1% of the assumed accretion power estimated by Yang et al. (2007). This shows that the  $[C II]$  line cooling in the inner parts of NGC 4258 is at least as important as the cooling from the hot X-ray plasma, although they are not strongly spatially correlated except in Regions Q and F.

How does the [C II] emission luminosity in Regions Q and F compare with the luminosity in the associated X-ray hotspots? We used *Chandra* X-ray observations<sup>17</sup> to estimate a soft (0.5–2 keV) X-ray luminosity of  $2.6 \times 10^{38}$  erg s<sup>-1</sup> and  $1.8 \times 10^{38}$  erg s<sup>-1</sup> respectively for Q and F. In comparison, our values of the [C II] line luminosity are  $7 \times 10^{38}$  erg s<sup>-1</sup> and  $1 \times 10^{39}$  erg s<sup>-1</sup>. Thus the ratio  $L([\text{C II}])/L(X_{0.5-2 \text{ keV}})$  for the two X-ray hotspots (Q, F) is therefore 2.7 and 5.6. As demonstrated by Ogle et al. (2014), heating of molecular gas by X-rays is very inefficient, and so these high values imply that the X-rays are not a dominant source of heating of the H<sub>2</sub> and [C II]-bright regions. More likely, both are providing evidence of significant cooling in shocked gas associated with the anomalous arms. Our fitting to the *Chandra* X-ray spectra showed that Region Q is consistent with a formally hotter plasma ( $kT = 0.64 \pm 0.05$  eV) than Region F ( $kT = 0.59 \pm 0.05$  eV), although only marginally so, within the uncertainties. This may imply a higher level of turbulent energy dissipation in Region Q if shocks are responsible. We recall that although Region Q radiates in the 0–0 S(1) H<sub>2</sub> line (the lowest H<sub>2</sub> transition in the ortho-H<sub>2</sub> rotational ladder), it is weak compared with the jet in NGC 4258. One explanation might be that the H<sub>2</sub> here is heated by stronger shocks than in the other regions, leading to a shifting of the H<sub>2</sub> power to much higher-energy rotational and rovibrational levels.

## 6. The Kinematics of the Minor-axis Filament

The [C II] emission from the minor-axis filament has an angular length of 30 arcsec (1 kpc at  $D = 7.3$  Mpc) and is blueshifted with respect to the nucleus ( $V_{\text{sys}} = 471.5 \pm 4$  km s<sup>-1</sup> from the nuclear maser disk; Miyoshi et al. 1995). The northern tip of the filament (see Figure 4) has a velocity centroid that peaks around 360–380 km s<sup>-1</sup>, which is an overall blueshift of 100 km s<sup>-1</sup> relative to the maser nucleus. It also exhibits broad line widths with the tip having a deconvolved FWHM of  $\sim 236$  km s<sup>-1</sup>. The H $\alpha$  blobs in the *HST* image of the filament appear as a distorted loop or partial ring, so some of the broad width could relate to a strong velocity gradient across the narrow loop. Its kinematics are incompatible with normal rotation around the galaxy, which would have velocities on the major axis similar to that of the nucleus.

We detected the minor-axis filament with the Palomar CWI integral field instrument, which has a higher spatial resolution ( $2.5 \times 1.0$  arcsec<sup>2</sup> pixels and average seeing of  $\sim 1$  arcsec) than the SOFIA data. Figure 11(a) shows the integrated CWI map of the H $\alpha$  emission superimposed on the *HST* image, confirming that the filament emits strongly in H $\alpha$ . We subtracted continuum from the map, averaged over channels on either side of the H $\alpha$  line. This worked well, except close to the nucleus where the lines become very broad. Those areas where the continuum subtraction is unreliable are denoted by the black ellipse on Figure 11(a). Nevertheless, Figure 11(a) provides a picture of the emission further from the nucleus.

To get a better idea of the kinematics of the emission, in Figure 11(b) we extract spectra from the positions marked with white circles, and fit the resulting H $\alpha$  line with Gaussian

profiles. The results of the fitting are presented in Table 2. The velocity resolution of the Palomar spectra is 60 km s<sup>-1</sup>, which is four times better than the SOFIA data. Figure 11(c) shows the radial velocity of the line centroid as a function of position along the filament. For reference, the horizontal lines show the best estimate of the systemic velocity of the nucleus from (i) the main component fitted to H $\alpha$  from position 7N (black line) and (ii) the systemic heliocentric velocity derived from the measurements of the inner  $<0.3$  pc H<sub>2</sub>O maser disk of Miyoshi et al. (1995).

In some cases, more than one velocity component was needed (Figure 11(c)). The tip of the filament (P1) is best fit with two narrow components, one (red square) close to the systemic velocity of the galaxy and one (blue triangle) blueshifted from it by 100 km s<sup>-1</sup>. The double-Gaussian components are separated by 100 km s<sup>-1</sup> and may explain the [C II] line broadening at the tip of the filament if the H $\alpha$  and [C II] originate in similar kinematic components. These results are broadly consistent with a long-slit spectrum along the minor axis by Rubin & Graham (1990) and the narrow-band Fabry–Perot observations of Cecil et al. (1992), although the latter observations do not show the full complexity of the multiple line components seen in our PCWI observations.

In Figure 11(c), the blue triangles show that one of the main Gaussian component shows a coherent decrease in blueshifted velocity as one proceeds toward the nucleus from P1 to P4. Closer in to the nucleus at P4–P6, multiple components are again seen. For example, the component associated with the green points in the figure near the nucleus is strongly blueshifted. This broad, blueshifted component may be associated with the AGN. The red squares in the figure near the nucleus denote an additional redshifted component.

Despite the complexity of the kinematics close to the nucleus, the channel maps in Figure 4 and the H $\alpha$  data from the PCWI observations show that the majority of the [C II]-emitting and ionized gas in the minor-axis filament is blueshifted with respect to the nucleus. A blueshift in this minor-axis emission suggests radial motions. If we interpret the dark dust lanes south of the nucleus to indicate the side closest to the observer, then from the general east-to-west rotation of the galaxy we would expect the spin axis of the galaxy to point slightly toward us. If the filament is oriented close to this spin axis, the blueshift would imply an outflow. On the other hand, if the filament lies close to the disk plane, and lies beyond the center, the blueshift could be interpreted as inflow.

Can we estimate the total mass flow rate in the filament? From an analysis of the faint CO emission seen associated faintly with the filament (Krause et al. 2007), we measure a CO 1–0 line integral  $\Sigma S dV = 110 \pm 10$  Jy km s<sup>-1</sup>. For  $D = 7.3$  Mpc and assuming a Galactic value for  $X_{\text{CO}}$ , we find an H<sub>2</sub> mass of  $6 \times 10^7 M_{\odot}$ . If we assume that this is the dominant mass component in the filament and that the maximum time for the tip of the filament to fall onto (or flow out from) the disk is  $d_{\text{fil}}/\Delta V = 1 \text{ kpc}/100 \text{ km s}^{-1} \sim 10$  Myr (here  $d_{\text{fil}}$  is the linear scale of the filament and  $\Delta V$  is the difference in radial velocity between the tip of the filament and the galaxy system), we estimate a mass inflow (or outflow) rate of  $>6 M_{\odot} \text{ yr}^{-1}$ . This rate is a lower limit because we only measure the radial velocity component of the gas above the disk plane. For an assumed galaxy inclination of  $i = 64^{\circ}$  (Wilson et al. 2001), the outflow rate would be

<sup>17</sup> We extracted spectra for Regions F and Q in the two *Chandra* observations that include the area observed with SOFIA (ObsIDs 350 and 1618; PI: A. Wilson). Each combined spectrum (containing 319 and 355 source photons, respectively) was fit with a thermal model based on the Astrophysical Plasma Emission Code (Smith et al. 2001) with free metallicity absorbed by a Galactic foreground ( $N_{\text{H}} = 1.2 \times 10^{20} \text{ cm}^{-2}$ ; Dickey & Lockman 1990).

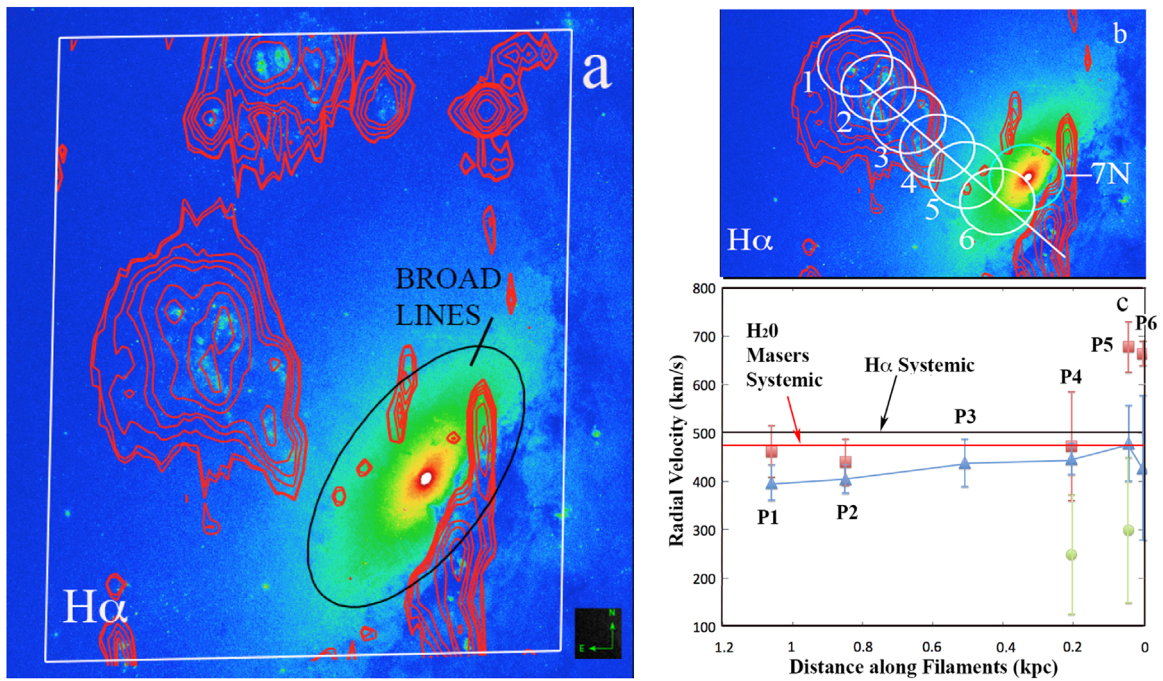


**Figure 11.** (a) Contours of the integrated  $H\alpha$  emission derived from the PCWI data cube superimposed on the *HST* image. The black ellipse shows the area around NGC 4258 where the  $H\alpha$  emission becomes very broad and the simple continuum subtraction, applied to make the contour maps, became less certain; (b) optical extraction regions P1–6 used to fit the  $H\alpha$  velocities to the data cube; (c) radial velocity of the filament as a function of distance along it, labeled by position in (b), based on fitting a Gaussian to each extracted spectrum (see Table 2 for details). The horizontal black and red lines show the heliocentric velocity of the galaxy measured from the PCWI ( $499 \pm 20 \text{ km s}^{-1}$ ) at the nucleus (marked 7N in (b)) and  $H_2O$  maser disk ( $471.5 \pm 4 \text{ km s}^{-1}$ ; Miyoshi et al. 1995). The size of the bars associated with each point shows the range of the FWHM for each fitted component. In several places, more than one component was required (blue triangles, red boxes, and green circles). One component (blue connected line) appears coherent along the filament from the tip at P1 to P5.

$6/\cos(i) = 14 M_{\odot} \text{ yr}^{-1}$  if the motion were perpendicular to the plane of the galaxy. If the filament flows in the plane of the galaxy, the inflow rate would be  $6/\sin(i) = 7 M_{\odot} \text{ yr}^{-1}$ .

### 7. A New Interpretation of the Jet/ISM Interactions in NGC 4258

With the exception of Region F, which is correlated with the bifurcation point in the radio and X-ray emission from the northern anomalous arms, the gas in the northern part of NGC 4258 has significantly smaller line widths and [C II]/PAH and [C II]/FIR ratios. Unlike the southern bow shock, a [C II] spectrum extracted near the position of the northern bow shock (Region D of Figure 5(b)) exhibits a narrow width (FWHM =  $144 \text{ km s}^{-1}$ ). The lack of a clear [C II] counterpart to the northern bow shock may suggest that the jet is passing through an ISM mainly devoid of gas, and may even have escaped from the disk. Unfortunately the amount of warm molecular gas associated with the northern bow shock cannot be tested at this time, since the *Spitzer* observations of warm  $H_2$  did not cover it. However, the lack of a dense obstacle in the path of the jet would be consistent with the fact that the northern bow shock is almost twice as far from the nucleus as the southern one, suggesting that the northern jet has experienced much less resistance in its forward progression through the galaxy.

Our SOFIA observations provide evidence that most of the [C II] emission south and southeast of the nucleus has the excitation and kinematic properties of gas that is likely shock-heated. The strongest emission, and that exhibiting the broadest [C II] line width, is associated with the southern jet bow shock, but the higher values of [C II]/PAH and [C II]/FIR occur further southeast, along a ridge defined by Regions M, N, O, and Q.

These areas coincide spatially with the braided  $H\alpha$  filaments of Cecil et al. (1992), which have optical emission-line ratios consistent with fast shocks. Interestingly, our [C II] line widths seem much broader than those seen in the optical Fabry–Perot observations, where the largest line width is  $80 \text{ km s}^{-1}$ . However, the kinematics and structure of the  $H\alpha$  filaments is quite complex here, as is apparent from the Fabry–Perot spectroscopy. For example, several different systemic velocity components are present, each representing a “braid” or filament (separated by  $\sim 200 \text{ km s}^{-1}$  in some cases).<sup>18</sup> It seems logical to assume that the broad [C II] lines we observe are a result of a complex network of shocks associated with a disturbed multiphase medium, of which the  $H\alpha$  filaments, X-ray, and radio-synchrotron emission are a part. We have modeled a similar multiphase medium in the case of Stephan’s Quintet (Guillard et al. 2009).

The existence of shocked emission beyond the tip of the southern bow shock begs the question of what is causing the shocks. Previous authors have considered several hypotheses to explain the existence and shape of the anomalous arms, including nuclear explosions (van der Kruit et al. 1972), previous jet outbursts confined to the plane of the galaxy (Cecil et al. 2000), and the radio/X-ray features being by-products of shocks created within the lighter halo gas by a jet that is currently pointing out of the plane of the disk by  $30^\circ$ . This latter model, presented by Wilson et al. (2001), assumes that the bow shocks are places where the current jet is colliding with rarefied halo gas. In the process of the jet propagating

<sup>18</sup> Unfortunately, bad weather did not allow us to investigate this region with our PCWI IFU observations.

**Table 2**  
Measurements of the PCWI H $\alpha$  Filament

Region <sup>a</sup>	$\lambda_{\text{cen1}}$ (Å)	$\Delta\lambda_1^b$ (Å)	$V_{\text{cen1}}$ (km s <sup>-1</sup> )	$\Delta V_1^b$ (km s <sup>-1</sup> )	$\lambda_{\text{cen2}}$ (Å)	$\Delta\lambda_2^b$ (Å)	$V_{\text{cen2}}$ (km s <sup>-1</sup> )	$\Delta V_2^b$ (km s <sup>-1</sup> )	$\lambda_{\text{cen3}}$ (Å)	$\Delta\lambda_3^b$ (Å)	$V_{\text{cen3}}$ (km s <sup>-1</sup> )	$\Delta V_3^b$ (km s <sup>-1</sup> )
1	6571.50	1.60	397	73	6572.91	2.34	462	106	...	...	...	...
2	6571.67	1.27	405	58	6572.43	2.10	440	96	...	...	...	...
3	6572.40	2.14	439	98	...	...	...	...	...	...	...	...
4	6572.57	1.39	446	63	6573.15	4.93	473	225	6568.22	2.39	248	109
5	6573.28	3.43	479	156	6577.64	2.28	678	104	6569.35	3.38	299	...
6	6572.17	6.56	428	299	6577.34	1.11	664	51	...	...	...	...
7N	6573.72	7.00	499	319	6576.73	1.31	636	60	...	...	...	...

**Notes.**

<sup>a</sup> Regions labeled in Figure 11.

<sup>b</sup> FWHM from observed line profile. Velocity resolution = 60 km s<sup>-1</sup>.

outward through that thin medium, shock waves are generated, which rain down onto the denser gaseous disk of NGC 4258 lying directly under the jet path, creating shocks and compression. One advantage of such a model is that it explains the offset in position angle between the jet and the ridge line of X-ray/radio emission in the inner anomalous arms (a result of a different projection of the jet and the disk onto the sky, as seen from the observer’s view; see Figure 9 of Wilson et al. 2001). However, this model does not convincingly explain the huge physical scale of the anomalous arms, which seem to extend well beyond any projected influence of the jet. Furthermore, the model does not explain why the anomalous arms are so symmetrical in both length and structure, especially given the different angular distances between the northern and southern bow shocks and the nucleus.

### 7.1. A Clumpy Thick-disk Schematic Picture of the ISM/Jet Interactions

The *Spitzer* and SOFIA observations presented here provide a further problem for the model of Wilson et al. (2001). Although, as we have discussed earlier, the northern segment of the jet is likely moving in a medium of lower density, the southern jet is not. It seems clear from both Figures 8(a, b) and 9 that the warm molecular hydrogen and the [C II] emission follow the southern jet closely, and the high velocity dispersion of the [C II] emission at the head of the southern jet suggests a direct influence of the jet on the warm H<sub>2</sub> and collisionally excited [C II] emission. This would not be expected if the jet were propagating through a rarefied halo gas.

Instead, we suggest a different explanation for the large extent of the (north and south) anomalous arms that involves the jet propagating into a clumpy thick disk containing many potential obstacles. We envisage a rotating thick disk containing a highly clumpy medium similar to the models of Wagner et al. (2012), but with the clouds confined to a narrower height within the potential. The jet in this picture would still be inclined to the disk, but by a smaller angle than that proposed by Wilson et al. (2001) in order for it to intersect with some of the disk clumps. Instead of the jets penetrating into the halo (as in the previous model), the clumps in the thick disk would act as obstacles to the jet, causing it to be significantly deflected, and confining the action to several channels both in the northern jet and to the south. The different behavior of the southern and northern structures near the jet therefore depends on what obstacles the jet encounters as it tries to push out through the clumpy medium. We postulate that the northern

part of the jet encountered, by chance, less clumpy material in its path until it reached its present location, compared with the southern jet, which is substantially stalled due to much more clumpy material in that direction. However, as the numerical models of Wagner et al. show, the existence of an obstacle does not stop the jet from being redirected around the obstacle, where it continues to encounter more clumps and experience further deflections. At each point in this process, shocks will be created both at the interface with the dense clouds and along the path where it passes through intercloud gas. Figure 1 of Wagner et al. (2012, central colored panel) is particularly illuminating. As the jet tries to pass through the clumpy galaxy, it encounters denser ISM clumps that deflect it, creating feathery structures that have remarkable similarity to the radio arms, with multiple bifurcation points where different clouds sometimes split the jet. In this picture, the anomalous arms of the jet are simply manifestations of the current jet, allowing for the possibility that the power can be redirected, especially in the southern jet. In the case of the northern jet, some extra refinements may be necessary because the radio emission first seems to follow the active jet but then seems to divert to the west before the bow shock is reached. In this case it might be that the jet has split there due to a small obstacle in the current flow or that the jet has not always pointed in the same direction in the recent past.

The models of Wagner et al. are for relatively powerful jets. For example, the lowest-power jet considered in their models had a power of  $P_{\text{jet}} = 10^{43}$  erg s<sup>-1</sup>. Yang et al. (2007) estimated the accretion power of the SMBH in NGC 4258 to be only  $4 \times 10^{41}$  erg s<sup>-1</sup>, which is 25 times lower than the lowest-power jet in the Wagner models, so is it reasonable to consider that the jet can be deflected around an obstacle if the jet is less powerful? First, the assumed accretion rate of  $7 \times 10^{-5} M_{\odot} \text{yr}^{-1}$ , upon which the accretion power is calculated, may be underestimated. For example, a much higher value of  $10^{-3} M_{\odot} \text{yr}^{-1}$  derived by Chary et al. (2000) was obtained based on the FIR spectral energy distribution. Furthermore, the jet power might depend on both the accretion rate and the spin of the black hole (Blandford & Znajek 1977; Nemmen et al. 2007), the latter of which is unknown. This would lead us to conclude that the jet power may be larger than originally assumed. It is also possible that the jet may have been more powerful in the past. Finally, even a lower-power jet can deposit significant amounts of energy into the ISM, but over a longer period of time (Mukherjee et al. 2016).

We admit that this picture is highly schematic, requires a relatively powerful jet, and will require a detailed model, beyond the scope of this paper, to demonstrate that it will work. However, even this simple picture has some advantages over previous models in explaining the *Spitzer* and SOFIA data. We have already discussed how this idea may explain the different lengths of the northern and southern jets. Moreover, it can also help us to understand the regions where we see the broad [C II] lines, southeast of the southern bow shock (Regions N, O, P, and Q). These might be places where the jet has been deflected into multiple strands or braids, where each braid seen in the Fabry–Perot imaging spectroscopy of Cecil et al. (1992) represents a separate channel of the main jet in that direction. These jet strands would likely shock-heat the gas more effectively than gas closer to the nucleus because they spread the jet energy over a larger volume of disk gas as the jet becomes successively split. Additionally, the molecular surface density is lower in these more distant parts of the galaxy, which will lead to generally faster shocks (and warmer gas) as the motion of the jet is less inhibited. As in our multi-ISM-phase modeling of the shocks in Stephan’s Quintet (Guillard et al. 2009, 2012a; Appleton et al. 2017), fast shocks (responsible for the optical emission-line ratios seen in the optical spectra) degrade rapidly, through a turbulent cascade, to slower shocks, which are capable of heating the molecular gas and generating [C II] emission. X-ray emission is also expected in these models, where the driving (in this case from the jets) compresses pockets of lower density material, which get heated to millions of degrees. However, if we are to capture all the observed complexities of the current observations, new modeling of a jet expanding into a clumpy disk with a declining surface density of molecular gas will be required.

## 8. Conclusions

We detect widespread [C II] emission in a highly irregular distribution in the inner 5 kpc of NGC 4258. The observations described in this paper lead to the following conclusions:

1. We demonstrate a close correspondence between the distribution of [C II] emission and shock-excited warm molecular hydrogen associated with the southern jet from the nucleus of NGC 4258. A re-analysis of the *Spitzer* IRS observations (originally reported by Ogle et al. 2014) shows an elongated structure of bright warm H<sub>2</sub> that follows the southern part of the jet and terminates in the southern jet bow shock. The [C II] emission shows a similar morphology but extends even further south and east into the area of lower surface brightness H<sub>2</sub>, in which complex braided H $\alpha$  shocked filaments were detected by previous work. Given the lack of powerful star formation along the jet, this strongly suggests that the [C II] transition is collisionally excited by the warm shock-heated molecular gas and not in PDRs. This is the first time shock-excited [C II] emission has been resolved along an AGN jet.
2. We also detect enhanced (compared with regions dominated by star formation) [C II] emission associated with X-ray and radio hotspots that are part of the inner anomalous spiral arms (Regions Q and F of Figure 5). Previous authors, using X-ray observations and optical

spectroscopy, have proposed that these anomalous arms are shock-heated regions somehow associated with the jet. Region Q shows an unusually high value of  $L([\text{C II}])/L(\text{FIR}) = 6.7\% \pm 1.1\%$ , and both Regions Q and F show very elevated values of  $L([\text{C II}])/L(\text{PAH})$  ratios compared with normal galaxies. These same regions exhibit unusually large [C II] line widths (many exceeding  $200 \text{ km s}^{-1}$ ). We propose that the rising ratios of  $L([\text{C II}])/L(\text{FIR})$  and  $L([\text{C II}])/L(\text{PAH})$  as one progresses further from the nucleus along the ridge of shocked gas to the southeast are a result of a radial decrease in the surface density of dust and PAHs. By contrast, the mechanical energy deposited into the gas from the jet does not decrease radially, leading to an apparent increase in [C II]/FIR and [C II]/PAH ratios, and broad lines. Unlike conditions in a PDR, in this picture the [C II] emission and the star formation indicators (FIR and PAH emission) are not correlated.

3. In two anomalous arm regions far from the nucleus, the  $L[\text{C II}]/L(\text{soft X-ray})$  ratio is large (2.7 and 5.6 in Q and F respectively), ruling out direct heating of the H<sub>2</sub> and [C II] gas by X-rays. Rather, the X-ray, H<sub>2</sub>, and [C II] emissions likely all arise in shocks in a multiphase medium (e.g., Guillard et al. 2009). On the other hand, in the nucleus and in a region along the northern jet, X-rays or strong UV radiation may have reduced the strength of [C II] emission (leading to a [C II]/FIR decrement), perhaps as a result of the gas being illuminated by hard radiation from the hot accretion disk.
4. As with previous studies of ionized gas in NGC 4258, the inner 5 kpc of NGC 4258 in [C II] emission has a highly disturbed velocity field with little semblance of normal rotation. In addition, the line widths of most of the [C II] emission, after correction for instrumental broadening, are broad (from FWHM of  $118\text{--}455 \text{ km s}^{-1}$ ), with the largest line width corresponding to the region where the southern jet exhibits a bow shock at optical wavelengths. This supports the idea that the jet is creating widespread turbulence and shocks that deposit energy into the ISM.
5. We detect [C II] emission from a minor-axis filament extending 30 arcsec (1 kpc) from the nucleus, which is associated with a loop of bright H $\alpha$ -emitting star formation regions. The [C II] emission from the filament coincides with bright PAH emission detected with *Spitzer* and likely arises in PDRs associated with faint molecular gas. Follow-up observations with the Palomar CWI IFU suggests that the filament represents gas blueshifted relative to the nucleus. Depending on its 3D orientation relative to the disk plane, the filament is either falling onto or expanding away from the disk. Its potential relationship to the nuclear activity in NGC 4258 is currently unknown.
6. Up to 40% of the luminosity in the [C II]-emitting gas can be attributed to emission that is likely dominated by shocks and turbulence ( $[\text{C II}]/\text{PAH}$  percentages  $>10\%$ ) rather than emission attributed to star formation activity. We estimate that the jet is depositing  $3.8 \times 10^{39} \text{ erg s}^{-1}$  into the gas, which cools through [C II] emission, which is  $\leq 1\%$  of the estimated jet power. This is comparable to the integrated soft X-ray emission from the inner anomalous arms. Such large fractional luminosity of

shocked [C II] emission in a nearby AGN has implications for interpreting [C II] luminosity of high- $z$  galaxies, where turbulence and feedback effects from star formation and AGNs probably play an important role in galaxy evolution.

7. We propose a schematic picture, based on analogy with numerical models, in which the jet is propagating through a thick disk composed of a clumpy medium. In this picture, the northern jet has encountered less dense obstacles, allowing it to move further into the galaxy. By contrast, the southern portion of the jet has impacted much denser material, explaining the shorter jet length and the existence of significant amounts of molecular H<sub>2</sub> and [C II] emission around the southern bow-shock region. Models show that, if the jet is powerful enough, it will find ways around a given obstacle, creating further shocks and jet bifurcations and peculiar filaments downstream. This is consistent with the detection of [C II] emission in regions free of star formation, broad line widths, and peculiar H $\alpha$  filaments seen by previous authors. In this picture, the anomalous radio arms are places of generally lower density, mainly downstream of the main obstructions, where the jet has been deflected through potentially multiple interactions with clumps in a thick disk. As such, the anomalous arms are not relics of past activity but are places where the jet is still actively depositing energy despite having been deflected from the main bow-shock regions.

Results in this paper are based on observations made with the NASA/DLR Stratospheric Observatory for Infrared Astronomy (SOFIA). SOFIA is jointly operated by the Universities Space Research Association, Inc. (USRA), under NASA contract NAS2-97001, and the Deutsches SOFIA Institut (DSI) under DLR contract 50-OK-0901 to the University of Stuttgart. Financial support for this work was provided by NASA through awards SOF-04-0205 and SOF-05-0014, issued by USRA. The authors wish to thank an anonymous referee for very useful comments. Parts of the observations described in this paper were obtained at the Hale Telescope, Palomar Observatory, as part of a continuing collaboration between the California Institute of Technology, NASA/JPL, Yale University, and the National Astronomical Observatories of China. The authors wish to thank Chris Martin, the CWI team, and the staff of the Palomar observatory for permission to use, and assistance with, the semi-private PCWI instrument. The authors also thank S. Laine (Caltech/IPAC) and M. Krause (MPIFR) for permission to use the radio continuum, CO 1–0, and processed IRAC images used in this paper. This work was initiated, in part, at the Aspen Center for Physics, which is supported by NSF grant PHY-1607611. T.D.-S. acknowledges support from ALMA-CONICYT project 31130005 and FONDE-CYT regular project 1151239.

### ORCID iDs

P. N. Appleton  <https://orcid.org/0000-0002-7607-8766>  
 T. Diaz-Santos  <https://orcid.org/0000-0003-0699-6083>  
 D. Fadda  <https://orcid.org/0000-0002-3698-7076>  
 P. Ogle  <https://orcid.org/0000-0002-3471-981X>  
 A. Togi  <https://orcid.org/0000-0001-5042-3421>  
 L. Lanz  <https://orcid.org/0000-0002-3249-8224>  
 K. Alatalo  <https://orcid.org/0000-0002-4261-2326>

C. Fischer  <https://orcid.org/0000-0002-7299-8661>  
 J. Rich  <https://orcid.org/0000-0002-5807-5078>  
 P. Guillard  <https://orcid.org/0000-0002-2421-1350>

### References

- Abel, N. P., Dudley, C., Fischer, J., Satyapal, S., & van Hoof, P. A. M. 2009, *ApJ*, 701, 1147
- Alatalo, K., Appleton, P. N., Lisenfeld, U., et al. 2014, *ApJ*, 795, 159
- Appleton, P. N., Guillard, P., Boulanger, F., et al. 2013, *ApJ*, 777, 66
- Appleton, P. N., Guillard, P., Togi, A., et al. 2017, *ApJ*, 836, 76
- Appleton, P. N., Xu, K. C., Reach, W., et al. 2006, *ApJL*, 639, L51
- Armus, L., Mazzarella, J. M., Evans, A. S., et al. 2009, *PASP*, 121, 559
- Beirão, P., Armus, L., Helou, G., et al. 2012, *ApJ*, 751, 144
- Blandford, R. D., & Znajek, R. L. 1977, *MNRAS*, 179, 433
- Cecil, G., Greenhill, L. J., DePree, C. G., et al. 2000, *ApJ*, 536, 675
- Cecil, G., Wilson, A. S., & Tully, R. B. 1992, *ApJ*, 390, 365
- Chary, R., Becklin, E. E., Evans, A. S., et al. 2000, *ApJ*, 531, 756
- Cluver, M. E., Appleton, P. N., Boulanger, F., et al. 2010, *ApJ*, 710, 248
- Cormier, D., Madden, S. C., Leboutteiller, V., et al. 2015, *A&A*, 578, A53
- Croxall, K. V., Smith, J. D., Wolfire, M. G., et al. 2012, *ApJ*, 747, 81
- Díaz-Santos, T., Armus, L., Charmandaris, V., et al. 2013, *ApJ*, 774, 68
- Díaz-Santos, T., Armus, L., Charmandaris, V., et al. 2014, *ApJL*, 788, 17
- Díaz-Santos, T., Armus, L., Charmandaris, V., et al. 2017, *ApJ*, 846, 32
- Dickey, J. M., & Lockman, F. J. 1990, *ARA&A*, 28, 215
- Draine, B. T. 1978, *ApJS*, 36, 595
- Erickson, E. F., & Davidson, J. A. 1993, *AdSpR*, 13, 549
- Fadda, D., & Chambers, E. T. 2018, AAS Meeting 231, 150.11
- Fischer, C., Beckmann, A., Colditz, S., et al. 2018, *JAI*, 7, 1840003
- Fischer, J., Abel, N. P., González-Alfonso, E., et al. 2014, *ApJ*, 795, 117
- Goldsmith, P. F., Langer, W. D., Pineda, J. L., & Velusamy, T. 2012, *ApJS*, 203, 13
- González-Alfonso, E., Smith, H. A., Fischer, J., & Cernicharo, J. 2004, *ApJ*, 613, 247
- Graciá-Carpio, J., Sturm, E., Hailey-Dunsheath, S., et al. 2011, *ApJ*, 728L, 7
- Greenhill, L. J., Jiang, D. R., Moran, J. M., et al. 1995, *ApJ*, 440, 619
- Guillard, P., Boulanger, F., Lehnert, M. D., et al. 2015, *A&A*, 574, A32
- Guillard, P., Boulanger, F., Pineau des Forêts, G., et al. 2012a, *ApJ*, 749, 158
- Guillard, P., Boulanger, F., Pineau Des Forêts, G., & Appleton, P. N. 2009, *A&A*, 502, 515
- Guillard, P., Ogle, P. M., Emonts, B. H. C., et al. 2012b, *ApJ*, 747, 95
- Habart, E., Boulanger, F., Verstraete, L., et al. 2003, *A&A*, 397, 623
- Helou, G., Roussel, H., Appleton, P., et al. 2004, *ApJS*, 154, 253
- Herrera-Camus, R., Bolatto, A. D., Wolfire, M. G., et al. 2015, *ApJ*, 800, 1
- Herrera-Camus, R., Sturm, E., Graciá-Carpio, J., et al. 2018, *ApJ*, 861, 94
- Hollenbach, D., & McKee, C. F. 1989, *ApJ*, 342, 306
- Kaufman, M. J., Wolfire, M. G., Hollenbach, D. J., & Luhman, M. L. 1999, *ApJ*, 527, 795
- Klein, R., Beckmann, S., Bryant, A., et al. 2014, *Proc. SPIE*, 9147, 91472X
- Krause, M., Fendt, C., & Neining, N. 2007, *A&A*, 467, 1037
- Laine, S., Krause, M., Tabatabaei, F. S., & Siopis, C. 2010, *AJ*, 140, 1084
- Langer, W. D., & Pineda, J. L. 2015, *A&A*, 580, A5
- Lanz, L., Ogle, P. M., Alatalo, K., & Appleton, P. N. 2016, *ApJ*, 826, 29
- Lanz, L., Ogle, P. M., Evans, D., et al. 2015, *ApJ*, 801, 17
- Lesaffre, P., Pineau des Forêts, G., Godard, B., et al. 2013, *A&A*, 550, A106
- Looney, L. W., Geis, N., Genzel, R., et al. 2000, *Proc. SPIE*, 4014, 14
- Lord, S. D. 1992, NASA Technical Memorandum 103957, <https://ntrs.nasa.gov/archive/nasa/casi.ntrs.nasa.gov/19930010877.pdf>
- Lutz, D., Berta, S., Contursi, A., et al. 2016, *A&A*, 591, A136
- Malhotra, S., Helou, G., Stacey, G., et al. 1997, *ApJL*, 491, 27
- Malhotra, S., Kaufman, M. J., Hollenbach, D., et al. 2001, *ApJ*, 561, 766
- Miyoshi, M., Moran, J., Herrnstein, J., et al. 1995, *Natur*, 373, 127
- Mukherjee, D., Bicknell, G. V., Sutherland, R., & Wagner, A. 2016, *MNRAS*, 461, 967
- Negishi, T., Onaka, T., Chan, K.-W., & Roellig, T. L. 2001, *A&A*, 375, 566
- Nemmen, R. S., Bower, R. G., Babul, A., & Storchi-Bergmann, T. 2007, *MNRAS*, 377, 1652
- Neufeld, D. A., & Maloney, P. R. 1995, *ApJL*, 447, L17
- Ogle, P., Antonucci, R., Appleton, P. N., & Whysong, D. 2007, *ApJ*, 668, 699
- Ogle, P., Boulanger, F., Guillard, P., et al. 2010, *ApJ*, 724, 1193
- Ogle, P. M., Lanz, L., & Appleton, P. N. 2014, *ApJL*, 788, L33
- Peterson, B. W., Appleton, P. N., Bitsakis, T., et al. 2018, *ApJ*, 855, 141
- Rahman, S., Martin, C., McLean, R., Matuszewski, M., & Chang, D. 2006, *Proc. SPIE*, 6269, 62693W

- Rubin, V. C., & Graham, J. A. 1990, [ApJL](#), **362**, L5
- Smith, J. D. T., Armus, L., Dale, D. A., et al. 2007, [PASP](#), **119**, 1133
- Smith, J. D. T., Croxall, K., Draine, B., et al. 2017, [ApJ](#), **834**, 5
- Smith, R. K., Brickhouse, N. S., Liedahl, D. A., & Raymond, J. C. 2001, [ApJL](#), **556**, L91
- Spilker, J. S., Marrone, D. P., Aravena, M., et al. 2016, [ApJ](#), **826**, 112
- Stacey, G. J., Hailey-Dunsheath, S., Ferkinhoff, C., et al. 2010, [ApJ](#), **724**, 597
- Tielens, A. G. G. M., & Hollenbach, D. 1985, [ApJ](#), **291**, 722
- van Albada, G. D., & van der Hulst, J. M. 1982, [A&A](#), **115**, 263
- van der Kruit, P. C., Oort, J. H., & Mathewson, D. S. 1972, [A&A](#), **21**, 179
- Voit, G. M. 1992, [ApJ](#), **299**, 495
- Wagner, A. Y., Bicknell, G. V., & Umemura, M. 2012, [ApJ](#), **757**, 136
- Wilson, A. S., Yang, Y., & Cecil, G. 2001, [ApJ](#), **560**, 689
- Wolfire, M. G., Tielens, A. G. G. M., & Hollenbach, D. 1990, [ApJ](#), **358**, 116
- Yang, Y., Li, B., Wilson, A. S., & Reynolds, C. S. 2007, [ApJ](#), **660**, 1106